

1 Role of Indian Ocean basin mode in driving the interdecadal 2 variations of summer precipitation over the East Asian monsoon 3 boundary zone

4
5 Jing Wang^{1,*}, Yanju Liu², Fei Cheng^{3,*}, Chengyu Song⁴, Qiaoping Li⁵, Yihui Ding², Xiangde Xu⁶

6 ¹Tianjin Key Laboratory for Oceanic Meteorology, and Tianjin Institute of Meteorological Science, Tianjin, China

7 ²National Climate Center, China Meteorological Administration, Beijing, China

8 ³Ningbo Meteorological Observatory, Ningbo, China

9 ⁴Heilongjiang Climate Centre, Harbin, China

10 ⁵CMA Earth System Modelling and Prediction Centre, Beijing, China

11 ⁶State Key Laboratory of Severe Weather, Chinese Academy of Meteorological Sciences, Beijing, China

12
13 Correspondence: Yanju Liu (liuyan@cmac.gov.cn)

14 * Jing Wang and Fei Cheng contributed equally to this work.

15
16 **Abstract.** Based on long-term observational and reanalysis datasets from 1901 through 2014, this study investigates the
17 characteristics and physical causes of the interdecadal variations in the summer precipitation over the East Asian monsoon
18 boundary zone (EAMBZ), which is a peculiar domain defined from the perspective of the interplay between climatic
19 systems (i.e., mid-latitude westerly and East Asian summer monsoon). Observational evidence reveals that, similarly to
20 previous studies, the EAMBZ precipitation featured prominent interdecadal fluctuations, e.g., with dry summers during
21 the periods preceding 1927, 1939–1945, 1968–1982, and 1998–2010, and wet summers during the periods of 1928–1938,
22 1946–1967, and 2011 onwards. Further analyses identify that, amongst the major interdecadal oceanic forcings (e.g.,
23 Atlantic multidecadal oscillation and Pacific decadal oscillation), the Indian Ocean basin mode (IOBM) is a significant
24 oceanic forcing responsible for the interdecadal variations of the EAMBZ precipitation, playing an independent and
25 critical modulation role. When the cold phase of the IOBM occurs, an anomalous cyclonic circulation is excited around
26 the northeast corner of the tropical Indian Ocean, which further induces a “north-low–south-high” meridional seesaw
27 pattern over the Northeast China–subtropical western Pacific (SWP) sector. Such seesaw pattern is conducive to the
28 enhanced EAMBZ precipitation through linking favorable environments for the transportation of water vapor from the
29 SWP and the convergence over EAMBZ at interdecadal timescales. For this reason, a physical-empirical model for the
30 EAMBZ precipitation is developed in terms of the IOBM cooling. Despite the fact that the extreme summer EAMBZ
31 precipitation cannot be captured by this model, it can still well capture its interdecadal fluctuations and reflect their steady
32 relationship. The key physical pathway connecting the IOBM cooling with the interdecadal variations of the summer
33 EAMBZ precipitation is supported by the numerical results based on the large ensemble experiment and the Indian Ocean
34 pacemaker experiment. Our findings may provide new insights into the understanding of the causes of the interdecadal
35 variations in the summer EAMBZ precipitation, which may favor the long-term policy decision making for the local
36 hydrometeorological planning.

37 38 1 Introduction

39
40 The monsoonal airflows and mid-latitude westerlies are crucial components of the Asian climate system (Li and Zeng,
41 2002; Ding and Chan, 2005; Wang et al., 2008; Wu et al., 2012; Huang et al., 2015; Wang et al., 2017; Chen et al., 2018;
42 J. Huang et al., 2019). These two subsystems can synergistically induce regional precipitation fluctuations over
43 subtropical and mid-latitude Asia during the Northern Hemisphere late spring (May) and summer (June–July–August;

44 JJA) (Qian et al., 2009; Chen et al., 2021; Song et al., 2022; J. Wang et al., 2022). For example, Song et al. (2022) found
45 that May precipitation over the southeastern extension of the Tibetan Plateau (TP) features notable year-to-year variations,
46 which are physically linked to a unique interplay between the upstream mid-latitude westerlies and the Bay of Bengal
47 summer monsoon.

48
49 During the early stage of the northern summer, however, the mid-latitude -westerlies shift poleward to the north of the TP
50 abruptly (Yeh et al., 1959; Schiemann et al., 2009). In this context, westerlies of mid-latitude synoptic disturbance and
51 southerlies of East Asian summer monsoon (EASM) collide with each other frequently over the East Asian monsoon
52 boundary zone (EAMBZ) (Qian et al., 2009; Wang et al., 2017; Chen et al., 2018; J. Huang et al., 2019; Zeng and Zhang,
53 2019; Chen et al., 2021; Q. Wang et al., 2021, 2022, 2023). It is essential to point out that although the EAMBZ domain
54 largely overlaps the Northeast Asian area suggested by Si et al. (2021), the EAMBZ is defined from the perspective of
55 the interaction between the mid-latitude westerly and the EASM [see Fig. 1 in Chen et al. (2021); also see the red box in
56 Fig. 1 and associated description in Sect. 2.5.1], not from a geographical notion. Accordingly, the EAMBZ is a transitional
57 climate zone between the EASM-controlled moist region and the westerly-dominated arid region over central Asia (Chen
58 et al., 2010; Chen et al., 2018, 2021), stretching from the eastern flank of the TP to Mongolia and Northeast China. Notably,
59 EAMBZ is a distinguished region with agrarian economy and animal husbandry, which is largely susceptible to water
60 resource variations (Ou and Qian, 2006; Lu and Jia, 2013). Nevertheless, many studies reported that in the past century,
61 the semi-arid EAMBZ underwent the most profound warming over East Asia, suffering from serious aridification and a
62 high risk of desertification (J. Huang et al., 2017, 2019, 2020). In this regard, EAMBZ is deemed one of the “hotspots”
63 highly sensitive to precipitation fluctuations (Qian et al., 2009; Lu and Jia, 2013; J. Huang et al., 2019). Given that the
64 EAMBZ is of an ecologically fragile environment with water shortage, a deep understanding of the reasons for historical
65 changes in summer EAMBZ precipitation could be a prerequisite for in situ ecological improvement and socioeconomic
66 development.

67
68 Existing studies have well documented physical mechanisms responsible for the interannual variability of summer
69 EAMBZ precipitation, highlighting the external moisture supply pathways, the modulators for the wet-dry condition
70 variations [e.g., the mid-latitude westerlies within the Asian westerly jet, the western North Pacific subtropical high, and
71 the EASM], and the remote modulation roles of large-scale teleconnected modes [e.g., Silk Road pattern/circumglobal
72 teleconnection propagating along the westerly jet and the Eurasian teleconnection] and sea surface temperature (SST)
73 anomaly patterns (Huang et al., 2015; Wang et al., 2017; Chen et al., 2018, 2021; Zhao et al., 2019a, 2019b, 2020; Q.
74 Wang et al., 2021, 2022, 2023). For instance, Q. Wang et al. (2022) suggested that the positive phase of the Eurasian
75 teleconnection is connected with a low pressure anomaly in the lower troposphere in EAMBZ and the Mongolia region,
76 thus favoring enhanced summertime precipitation over EAMBZ; and meanwhile, the circumglobal teleconnection is
77 positively coupled with the EAMBZ precipitation, with ascending motion anomalies over EAMBZ during its positive
78 phase. Chen et al. (2021) established that the circulations (i.e., the mid-latitude westerlies and EASM) and the forcing of
79 SST anomalies (SSTAs) can collectively regulate the summer EAMBZ precipitation variability. The variability of
80 westerlies is largely modulated by the Silk Road pattern and the meridional displacement of the westerly jet; while the
81 EASM variability is mainly modulated by the prior wintertime El Niño-Southern Oscillation. The synchronized effects
82 of EASM and westerlies largely contribute to the rainfall variability in EAMBZ. Note that Chen et al. (2021) also pointed
83 out that the Indian Ocean basin mode (IOBM) is simultaneously correlated with the EASM in boreal summer on the
84 interannual timescale, which may be considered as a salient oceanic modulator for the summer EAMBZ precipitation
85 variability. Nevertheless, they paid little attention to the physical mechanisms of how IOBM regulates the year-to-year
86 EAMBZ precipitation. Moreover, Zhao et al. (2019a) found that the tropical northern Atlantic SSTAs have significant

87 impacts on the August rainfall over the monsoon transitional zone in China through inducing a wavetrain over Eurasia
88 and the western North Pacific anomalous anticyclone.

89

90 Compared with the extensively explored interannual variability of the JJA EAMBZ precipitation, less efforts have been
91 devoted to its interdecadal variability. To understand and predict the summer EAMBZ precipitation, exploring its
92 interdecadal variations and the underlying physical causes are also critical, which is the main focus of the present study.
93 Previous studies suggested that the warm-season precipitation over many Asian areas features interdecadal fluctuations.
94 For example, J. Wang et al. (2022) reported that the late spring (May) southeastern TP underwent wet conditions for
95 1928–1961 and 1989–2003, and experienced dry conditions preceding 1927, 1962–1988, and 2004 onwards. Si and Ding
96 (2016) documented that East Asia experienced dry summers from the early 1920s to the 1940s, while wet summers from
97 the late 1900s to the early 1920s, in the 1950s, and from the 1980s to the 1990s. Piao et al. (2021) found that the decadal-
98 filtered summer precipitation over Northeast Asia underwent a sudden decrease around the late 1990s. The interdecadal
99 oceanic forcings for the interdecadal changes of the Asian summer rainfall are also extensively investigated, highlighting
100 the crucial modulation roles of basin-scale SST modes of Atlantic multidecadal oscillation (Si et al., 2021), Pacific decadal
101 oscillation/interdecadal Pacific oscillation (IPO) (Si and Ding, 2016), and IOBM (Zhang et al., 2018). Among these
102 interdecadal oceanic forcings, it is essential to emphasize the IOBM, a dominant mode of SST variability in the tropical
103 Indian Ocean (TIO) sector, which usually follows up a wintertime El Niño-Southern Oscillation event and persists into
104 the summer through the capacitor effect (Klein et al., 1999; Yang et al., 2007; Xie et al., 2009). It is worth noting that the
105 IOBM also features a basin-scale warming/cooling at interdecadal timescales (Han et al., 2014), exerting active impacts
106 on the mid-latitude Asian climate (e.g., Wu et al., 2016; Li and Ma, 2018; Zhang et al., 2018; S. Wang et al., 2022). As
107 for the interdecadal variations of the summer EAMBZ precipitation, we hope to answer the following two questions: 1)
108 Did the JJA EAMBZ precipitation feature interdecadal variations? If so, 2) is there any intimate connection between
109 IOBM and the EAMBZ precipitation at interdecadal timescales? As such, this study shall extend previous studies by
110 exploring what extent and how the JJA IOBM modulate the concurrent EAMBZ precipitation variability at interdecadal
111 timescales, with the aim of providing a novel understanding for the rainfall variability over the mid-latitude semi-arid
112 zone in Asia. Note that we employ datasets with a centennial scale in this study [e.g., the precipitation data produced by
113 the Climatic Research Unit (CRU) and the atmospheric circulation data from the Twentieth Century Reanalysis datasets].
114 In comparison with the short-term datasets since the latter half of the 20th century, these long-term datasets can separate
115 the interdecadal variability of EAMBZ precipitation from the externally forced global climate change caused by
116 anthropogenic (e.g., greenhouse gas) and natural forcings (e.g., volcanic eruption) more effectively (Wu et al., 2016),
117 which were widely used to investigate the physical causes of how internal fluctuations of the climate system modulate
118 the interdecadal variations of precipitation over Asia (e.g., Wu et al., 2016; Zhang et al., 2018; Sun et al., 2019a; Jiang et
119 al., 2021; J. Wang et al., 2022).

120

121 The remainder of this paper is arranged as follows. Section 2 describes the datasets and methods used in this study. Section
122 3 elucidates the characteristics of the interdecadal variations of summertime EAMBZ precipitation and the associated
123 background circulations, illustrates the mechanisms of how IOBM modulates the EAMBZ precipitation, establishes a
124 linear regression model using the IOBM to predict the interdecadal precipitation anomalies over EAMBZ, and verifies
125 the IOBM-related physical processes using numerical model simulations. A summary of the major findings and further
126 discussions are provided in Section 4.

127

128 2 Datasets and methods

129

130 2.1 Observational Data

131

132 Several monthly mean observational datasets are utilized in the present study, including (1) the global land high-resolution
133 gridded CRU time series precipitation dataset version 3.26 (CRU TS3.26; spatial resolution: $0.5^\circ \times 0.5^\circ$; Harris et al., 2014)
134 for 1901–2017, (2) the Extended Reconstructed SST version 5 (ERSSTv5; spatial resolution: $2^\circ \times 2^\circ$; B. Huang et al., 2017)
135 for 1854–present derived from the National Oceanic and Atmospheric Administration (NOAA), and (3) atmospheric
136 variables derived from NOAA–Cooperative Institute for Research in Environmental Sciences (CIRES) Twentieth Century
137 Reanalysis version 2c (20CRv2c; spatial resolution: $2^\circ \times 2^\circ$; Compo et al., 2011), except for the precipitation data, with
138 192 points in longitude and 94 points in latitude, for 1851–2014. Note that all observational datasets cover the common
139 time period of 1901–2014, which is the focused period in the present research.

140

141 2.2 Rossby wave source

142

143 Following Sardeshmukh and Hoskins (1988), the Rossby wave source (RWS) is calculated as:

$$144 \quad RWS = -\nabla \cdot [\mathbf{V}_\chi (\zeta + f)], \quad (1)$$

145 where \mathbf{V}_χ is the divergent wind, ζ is the relative vorticity, and f is the planetary vorticity.

146

147 2.3 Moisture flux and associated divergence

148

149 The vertically integrated horizontal water vapor transport ($\langle WVT \rangle$) and WVT-associated divergence ($\langle WVT_div \rangle$) are
150 calculated using the following equations (Sun et al., 2019b; J. Wang et al., 2022):

$$151 \quad \langle WVT \rangle = -\frac{1}{g} \int_{P_s}^{300} q \vec{V} dp, \quad (2)$$

$$152 \quad \langle WVT_div \rangle = -\frac{1}{g} \int_{P_s}^{300} \nabla_p \cdot (q \vec{V}) dp, \quad (3)$$

153 where $\nabla_p \cdot ()$ denotes the horizontal divergence in the pressure coordinates; g is the gravitational acceleration; P_s is the

154 surface pressure; q is the specific humidity; and $\vec{V} = (u, v)$ is the horizontal wind vector (u and v represent the zonal and

155 meridional winds, respectively).

156

157 2.4 Statistical methods

158

159 This study focuses on interdecadal fluctuations in variables. The data are 11-year low-pass filtered by adopting a Lanczos
160 filter (Duchon, 1979) to extract the corresponding interdecadal signal. Several statistical methods are used, including
161 empirical orthogonal function (EOF) analysis, composite analysis, correlation analysis, and linear regression analysis. A
162 two-tailed Student's t test is used to evaluate the statistical significance. Considering the 11-year low-pass filtered method
163 can significantly reduce the degrees of freedom of the data, the following approximation is therefore deployed to calculate
164 the effective degrees of freedom (N^{eff}):

$$165 \quad \frac{1}{N^{eff}} \approx \frac{1}{N} + \frac{2}{N} \sum_{j=1}^N \frac{N-j}{N} \rho_{XX}(j) \rho_{YY}(j), \quad (4)$$

166 where N is the sample size, and $\rho_{XX}(j)$ and $\rho_{YY}(j)$ are the autocorrelations of two sampled time series X and Y ,
167 respectively, at time lag j (Li et al., 2013).

168

169 In this study, we focus on the boreal summer season (JJA). All variables in observations and model simulations are
170 linearly detrended before further calculations and analyses to exclude potential impacts of long-term trends.

171

172 2.5 Definitions

173

174 2.5.1 The research domain of EAMBZ

175

176 From the long-term (1901–2014) perspective of the climatological mean state of converged $\langle WVT \rangle$ and pronounced
177 precipitation over the mid-latitude Asia, the EAMBZ (box in Figs. 1a and 1b; 35°–55°N, 105°–130°E) is defined as the
178 collision and convergence zone between JJA dry westerly $\langle WVT \rangle$ and moist southwesterly $\langle WVT \rangle$ (Fig. 1a). As such,
179 there exist wetter conditions over the EASM-dominated part and drier conditions over the westerly-controlled part (Fig.
180 1b), suggesting the semi-arid transitional feature of EAMBZ (Xing and Wang, 2017). Our defined research domain of
181 EAMBZ largely matches the monsoon boundary zone defined by Chen et al. (2021), covering Inner Mongolia, Gansu,
182 Ningxia, Shaanxi, Shanxi, Hebei, Beijing, Tianjin, Shandong, Jilin, Liaoning, and Heilongjiang in China, as well as
183 eastern Mongolia and Korean peninsula. Note that our focused EAMBZ domain differs from the Northeast Asian domain
184 (29°–50°N, 108°–140°E) suggested by Si et al. (2021). Although they are extensively overlapped, the EAMBZ is located
185 more westward and northward, and defined from the perspective of the interplay between climatic systems, not from a
186 pure geographical perspective. Since the areal mean precipitation over EAMBZ in boreal summer is the highest of the
187 year accompanying the largest standard deviation (i.e., largest rainfall variability) (Fig. S1), the summer season is focused
188 in the present study.

189

190 2.5.2 Climate indices

191

192 The IOBM index (I_{IOBM}) is defined as areal mean SSTAs over the TIO domain of 20°S–20°N, 40°–100°E (Xie et al.,
193 2009). The IPO index is calculated using a method identical to that defined in Henley et al. (2015), that is, the difference
194 between SSTAs averaged over the central equatorial Pacific (10°S–10°N, 170°E–90°W) and the average of SSTAs in the
195 northwest (25°–45°N, 140°E–145°W) and the southwest Pacific (50°S–15°S, 150°E–160°W). In observations,
196 considering the coupled nature of IOBM and IPO at interdecadal timescales in boreal summer [cf. Fig. 2a in Wu et al.
197 (2016)], we hence remove the potential influence of the contemporaneous IPO on precipitation via eliminating the forcing
198 of IPO from the data of climate variables based on the partial regression technique, which is widely used in previous
199 studies (e.g., Dou and Wu, 2018; J. Wang et al., 2022).

200

201 2.6 Model simulations

202

203 To validate our proposed mechanisms of how the TIO SSTAs (i.e., IOBM-associated SSTAs) remotely modulate the
204 summer EAMBZ precipitation on interdecadal timescales, following the method of Zhang et al. (2019) and Yang et al.
205 (2020), we adopt monthly mean outputs from two experiments of the Community Earth System Model version 1 (CESM1),
206 which is a fully coupled Earth system model incorporating components of atmosphere, ocean, land, and sea ice (Hurrell
207 et al., 2013).

208

209 The first experiment is the CESM1 Large Ensemble Numerical Simulation (referred to as CESM1_LENS; Kay et al.,
210 2015). Among total 40 ensemble members in CESM1_LENS (Yang et al., 2020), we use the first 35 individual members
211 according to many previous studies (e.g., Touma et al., 2021; J. Wang et al., 2023), which were completed at the climate
212 modeling center of National Center for Atmospheric Research (NCAR). Note that all ensemble members in
213 CESM1_LENS were imposed with the same radiative forcing scenario (Taylor et al., 2012), with historical forcing for
214 1920–2005 and high-emission forcing scenario (i.e., Representative Concentration Pathway 8.5) for 2006–2080 (Moss et
215 al., 2010; Touma et al., 2021). The ensemble members were further generated with slightly differentiated perturbations
216 of atmospheric states (Kay et al., 2015; Touma et al., 2021). The second experiment is the CESM1 Indian Ocean
217 Pacemaker Ensemble Simulation (referred to as CESM1_IOPES), with 10 ensemble members (Zhang et al., 2019; Yang
218 et al., 2020). We adopt CESM1_IOPES to highlight the impact of SSTAs over the broader TIO domain (15 °S–15 °N,
219 African coast to 174 °E). For the convenience of subsequent calculations and analyses, the African coast is designated as
220 40 °E in this study, and a small change in the longitudes regarding the African coast may not affect the main results.

221
222 As indicated by Yang et al. (2020), the CESM1_LENS 35-member ensemble mean results can better provide an estimate
223 of the influence of the due to external perturbations such as greenhouse gases on the climate system. Furthermore, the 10-
224 member ensemble mean results in CESM1_IOPES contain the responses to both the time-evolving radiative forcing due
225 to external perturbations and the restored observed time-varying SSTAs over the above broader TIO domain (Yang et al.,
226 2020). Note that though the ozone forcing data used in CESM1_IOPES differ from those in CESM1_LENS, the
227 differences in the corresponding simulated tropical and extratropical climates were indistinguishable (e.g., Schneider et
228 al., 2015; Schneider and Deser, 2018; Zhang et al., 2019; Yang et al., 2020). Therefore, by subtracting the CESM1_LENS
229 ensemble mean from the CESM1_IOPES ensemble mean (i.e., removing the shared radiative forcing described above),
230 we can obtain the response of the climate system to the internal variability stemming from the time-varying SSTAs over
231 the specific TIO, isolating the intrinsic climate variability driven by TIO SSTAs through excluding the impacts of the
232 time-evolving external radiative forcing. More details about CESM1_LENS and CESM1_IOPES can be found in Kay et
233 al. (2015) and Yang et al. (2020), respectively. The variables employed here comprise precipitation and wind in
234 atmosphere component of Community Atmospheric Model version 5, with a spatial resolution of 1.25 ° in longitude and
235 0.9 ° in latitude; and SST in the ocean component of Parallel Ocean Program version 2, with 320 grids in longitude and
236 384 grids in latitude. Before further analyses, model outputs are interpolated at a resolution of 2 °×2 ° using a bilinear
237 interpolation method (Mastyło, 2013), identical to that of 20CRv2c. In the current study, we focus on the historical
238 simulation period of 1920–2005.

239
240 Here, it is important to stress the following two points. First, although the TIO domain in CESM1_IOPES is broader than
241 that for defining I_{IOBM} , there exist highly consistent temporal variations in SSTAs between them in observations (Fig. S2)
242 and simulations (Fig. S3) at interdecadal timescales, with temporal correlation coefficients (TCCs) of 0.93 and 0.87 ($P <$
243 0.01), respectively. Second, when selecting the SSTAs over the broader TIO domain (purple box in Fig. S4) as a metric,
244 it can be found that the observed (Fig. S4a) and modelled (Fig. S4b) large and intense loadings of the positive SSTAs are
245 still concentrated around the narrower TIO domain (black box in Fig. S4). As such, it is plausible to adopt the above-
246 mentioned Indian Ocean pacemaker experiment with broader TIO SSTAs to validate our proposed mechanisms tied to
247 the interdecadal IOBM variations.

248

249 3 Results

250

251 3.1 Observed interdecadal variations of the summer precipitation over EAMBZ and related

252 background circulations

253

254 Figure 1c plots the spatial distribution of the interdecadal standard deviation of precipitation. This distribution is quite
255 similar to that of the climatology (Fig. 1b), suggesting relatively strong (weak) interdecadal precipitation fluctuations
256 over the EASM-dominated (westerly-controlled) part of the EAMBZ. Moreover, we show the first EOF mode of JJA-
257 mean EAMBZ precipitation (Fig. 1d), which accounts for 28% of the total variance and distinguishes from the remaining
258 eigenvectors according to the criterion defined by North et al. (1982). The leading EOF mode bears close resemblance to
259 the standard deviation of the EAMBZ precipitation on interdecadal timescales (Figs. 1c and 1d), with larger loadings
260 occupying the Bohai Sea and Korean peninsula and their adjoining regions. The interdecadal TCC between the principal
261 component of the EOF1 and area-averaged precipitation over the research domain of EAMBZ (35° – 55° N, 105° – 130° E)
262 [EAMBZ precipitation index (I_{EAMBZP} for short); Fig. 1e] is 0.93 ($P < 0.001$). The aforementioned results indicate that
263 that our defined I_{EAMBZP} can serve as a good indicator of the predominant fluctuations in the precipitation anomalies over
264 EAMBZ at interdecadal timescales. As such, from the time series of 11-year low-passed filtered I_{EAMBZP} (Fig. 1e), we can
265 observe that the summer EAMBZ precipitation delineates notable interdecadal fluctuations. For example, EAMBZ
266 experienced dry summers during the periods preceding 1927, 1939–1945, 1968–1982, and 1998–2010, but underwent
267 wet summers during the periods of 1928–1938, 1946–1967, and 2011 onwards. Note that to some extent, the observed
268 major interdecadal fluctuation periods of summertime EAMBZ precipitation are dissimilar from those tied to summertime
269 Northeast Asian precipitation revealed by observations (1900–2012) from 11 local meteorological stations (Si et al., 2021),
270 e.g. the above-normal precipitation over EAMBZ (Fig. 1e) vs. the below-normal precipitation over Northeast Asia around
271 1990 (Si et al., 2021; their Fig. 2a).

272

273 Before examining the modulation of IOBM on the interdecadal EAMBZ precipitation fluctuations, it is essential to
274 scrutinize the JJA-mean I_{EAMBZP} -associated circulation anomalies. The highest mid-latitude positive correlation region
275 can be discerned north of the TP (38° – 46° N, 80° – 112.5° E; blue box in Fig. 2a), suggesting that the interdecadal
276 enhancement of the summer EAMBZ precipitation is intimately correlated with the acceleration of the upstream mid-
277 latitude westerlies at 400 hPa. In light of the method of Chen et al. (2021) and J. Wang et al. (2022), we correlate the
278 I_{EAMBZP} with the zonal winds averaged over the longitudinal range of EAMBZ at multiple levels (Fig. 2b) to further check
279 whether the most significant correlation occurs at 400 hPa. Evidently, on interdecadal timescales, the largest positive
280 correlation between precipitation and mid-latitude westerlies within 38° – 46° N does occur at the mid-tropospheric level
281 of 400 hPa, with a TCC of 0.46 ($P < 0.01$) between the I_{EAMBZP} and areal mean 400-hPa zonal winds over the upstream
282 westerly-dominated domain (Fig. 2c). Note that this correlation pattern exhibits a barotropic structure (Fig. 2b).
283 Additionally, we correlate the I_{EAMBZP} with the 850-hPa meridional winds. The I_{EAMBZP} is positively correlated with the
284 key monsoonal southerly domain east of the TP (25° – 33° N, 102.5° – 112.5° E; green box in Fig. 2d), which is located in
285 the western portion of the EASM domain (Ying et al., 2023). The interdecadal correlation pattern between meridional
286 winds and the summer EAMBZ precipitation at multiple levels exhibits a baroclinic structure, with the significant positive
287 correlations confined below 500 hPa (Fig. 2e). Note that the strongest positive correlation is detected at 850 hPa within
288 102.5° – 112.5° E, with a TCC of 0.63 (Fig. 2f; $P < 0.001$) between I_{EAMBZP} and areal mean 850-hPa meridional winds over
289 the key EASM-controlled domain (Fig. 2d).

290

291 Figure 3 gives the JJA-mean I_{EAMBZP} -regressed circulation anomalies at interdecadal timescales. The interdecadal
292 enhancement of the EAMBZ precipitation is significantly linked to a localized quasi-barotropic cyclonic (low-pressure)
293 anomaly. At 400 hPa, significant westerly anomalies prevail in its southern flank, inducing the acceleration of westerlies
294 upstream of EAMBZ (Fig. 3a). At 850 hPa, the enhanced EAMBZ precipitation is connected to a north-south meridional

295 seesaw pattern, with a significant anticyclonic (high-pressure) anomaly over the subtropical western Pacific (SWP) and a
296 significant cyclonic anomaly over EAMBZ (Fig. 3b), exhibiting a somewhat barotropic structure (Figs. 3a and 3b).
297 Significant southerly anomalies prevail in the western flank of this SWP clockwise gyre anomaly (SWPCGA). Moreover,
298 from the perspective of $\langle WVT \rangle$ (Fig. 3c), the magnitudes of southerly $\langle WVT \rangle$ anomalies over the key EASM-controlled
299 domain tied to the SWPCGA are much greater than the westerly $\langle WVT \rangle$ anomalies over the westerly-dominated domain.
300 Note that the southerly $\langle WVT \rangle$ anomalies are significantly divergent, pushing copious amounts of warm and moist vapor
301 over the SWP into EAMBZ. Then, with the aid of the local anticlockwise $\langle WVT \rangle$ gyre pattern (Fig. 3c), the EASM
302 southerlies from the low latitudes, which bring warm temperature advection anomalies, may easily collide with the mid-
303 level cold temperature advection anomalies brought by mid-latitude enhanced westerlies (Figs. 4a and 4b), manifesting
304 the extratropical–tropical interplay around EAMBZ on interdecadal timescales. Such interplay is basically aligned with
305 that on interannual timescales (cf. Chen et al., 2021). Under such environments, atmospheric instability over EAMBZ can
306 be triggered to generate in situ significant ascending motion anomalies responsible for increased precipitation (Fig. 5a).
307 Note that considering the greater magnitudes of anomalies of $\langle WVT \rangle$ and warm temperature advection connected to the
308 southerlies over the key EASM-controlled domain, we presume that the monsoonal southerlies play a predominant
309 dynamical role in the interdecadal enhancement of precipitation over EAMBZ. To verify this presumption, we further
310 propose an East Asian monsoon index (I_{MI} for short), defined as the areal mean meridional winds at 850 hPa over the key
311 monsoonal southerly domain, and a westerly index (I_{WI} for short), defined as the areal mean 400-hPa zonal winds over
312 the upstream westerly-dominated region. The I_{MI} -regressed results can well and realistically reproduce the magnitudes
313 and distributions of the anomalous upward motions tied to I_{EAMBZP} (Fig. 5b vs. 5a). However, the magnitudes of I_{WI} -
314 regressed results are highly weakened, along with the major loadings shifting more southward (Fig. 5c). Above results
315 could allow us to conclude that the anomalous southerlies over the key monsoonal southerly domain could be the
316 predominant driving factor for the interdecadal enhancement of summer EAMBZ precipitation, whereas the upstream
317 accelerated westerlies play a secondary dynamical amplification role.

318

319 3.2 Interdecadal relationship between IOBM and the summer EAMBZ precipitation

320

321 Many previous studies have substantiated that the IOBM can remotely modulate summer rainfall fluctuations over the
322 mid-latitude Asia at interdecadal timescales (e.g., Zhang et al., 2018; S. Wang et al., 2022; Wu et al., 2022). Note that the
323 existing studies primarily highlighted the impacts of IOBM on the summer rainfall variations over northwest portion of
324 the mid-latitude Asia a (e.g., S. Wang et al., 2022; Wu et al., 2022). As for the work of Zhang et al. (2018), although this
325 study focused the northeast portion of the mid-latitude Asia including the EAMBZ, it highlighted the combined roles of
326 IOBM, Atlantic multidecadal oscillation, and Pacific decadal oscillation. In the present study, however, we identify that
327 it is the IOBM that may exert profoundly simultaneous impacts on the interdecadal variations of the EAMBZ precipitation
328 in boreal summer, which will be revealed subsequently.

329

330 Figure 6a exhibits the correlation pattern between the JJA-mean I_{EAMBZP} and the contemporaneous global gridded SST at
331 interdecadal timescales. The most pronounced and significant correlations are found in the TIO sector, which largely
332 matches the domain for delineating the IOBM mode (black frame in Fig. 6a). There exists a salient out-of-phase
333 relationship between the interdecadal EAMBZ precipitation changes and the IOBM mode, with a TCC of -0.57 between
334 I_{EAMBZP} and I_{IOBM} (Fig. 6b; $P < 0.01$). This result suggests that IOBM warming (cooling) is significantly connected with
335 dry (wet) EAMBZ summers, which serves as a critical oceanic modulator. On interdecadal timescales, the IOBM can
336 remotely spark conducive dynamical circumstances for increased precipitation over EAMBZ, i.e., the collision between
337 cold and warm airflows around EAMBZ (Figs. 4c and 4d) and the locally significant convergent ascending motion

338 anomalies resembled those tied to the positive I_{EAMBZP} (Fig. 5d vs. 5a). However, the extratropical cold (tropical warm)
339 temperature advection anomalies west (south) of the EAMBZ, which are tied to the strengthened westerlies (southerlies),
340 are quite insignificant (significant) (Figs. 4c and 4d). This indicates that the IOBM may exerts a more profound influence
341 on the southerly wind anomalies over the EASM-controlled domain, which is more important for enhanced EAMBZ
342 precipitation; whereas the IOBM may insignificantly modulate the westerly anomalies over the westerly-dominated
343 region. The possible underlying mechanisms of how IOBM links the summertime circulation anomalies responsible for
344 the interdecadal fluctuations in the EAMBZ precipitation will be illuminated in the next subsection.

345

346 3.3 Possible mechanisms

347

348 Figure 7 shows partial regression of the JJA-mean anomalies of SST and large-scale precipitation over TIO and its
349 neighboring areas onto the I_{IOBM} at interdecadal timescales with the IPO forcing removed. Corresponding to higher I_{IOBM}
350 years, warm SSTAs cover almost all areas of TIO, with large loadings appearing in the central-southern TIO and relatively
351 small loadings appearing in the northern TIO (Fig. 7a), which are aligned with the previous studies (Wu et al., 2016; Y.
352 Huang et al., 2019). Moreover, there are striking suppressed precipitation around the northeast corner of the TIO domain
353 (Fig. 7b), suggesting profoundly localized atmospheric responses (viz. the release of regional anomalous atmospheric
354 cooling) to the warm TIO SSTAs. Note that corresponding to cold TIO SST years, there exist positive precipitation
355 anomalies around the northeast corner of TIO, suggesting the release of anomalous atmospheric heating (figure not
356 shown). Since the significant out-of-phase relationship between summertime IOBM and EAMBZ precipitation at
357 interdecadal timescales, we adopt negative I_{IOBM} -regressed patterns to express the influence of cold SSTAs over the TIO
358 region. Figure 8 displays the anomalous patterns of the RWS, velocity potential, and divergent horizontal winds regressed
359 onto the negative I_{IOBM} . The velocity potential anomalies with larger negative (positive) loadings in the upper (lower)
360 troposphere are concentrated surrounding the northeast corner of TIO. Under these circumstances, local upper (lower)
361 tropospheric divergence (convergence) and negative (positive) RWS anomalies can be observed (Fig. 8), suggesting
362 enhanced ascending motions and convection activities in situ and thereby exciting the localized increased
363 precipitation/atmospheric heating. The above results indicate that IOBM cooling may transmit its interdecadal influence
364 via the intermediate atmospheric bridge of enhanced convective activities around the northeast corner of TIO, exerting a
365 remote modulation on an interdecadal enhancement of the EAMBZ rainfall.

366

367 Next, we further discuss the physical pathway linking IOBM cooling with the far-reaching downstream circulation
368 anomalies responsible for the interdecadal enhancement of EAMBZ precipitation, as shown in Fig. 9. Because the
369 cyclonic anomaly at 400 hPa shifts more eastward compared to the I_{EAMBZP} -regressed counterpart (Fig. 9a vs. 3a), only
370 fractional westerly anomalies occupy the eastern part of the westerly-dominated region. The TCC between I_{IOBM} and I_{WI}
371 is nearly equal to zero ($r = -0.06$), thus linking the insignificant cold temperature advection displayed in Fig. 4c.
372 Nevertheless, in the lower troposphere, a “north-low–south-high” meridional seesaw pattern over the Northeast China–
373 SWP sector is found to be linked with IOBM cooling (Fig. 9b). Note that this negative I_{IOBM} -regressed seesaw pattern
374 exhibits a quasi-barotropic structure, with an anticlockwise $\langle WVT \rangle$ gyre in the north and a SWPCGA in the south (Fig.
375 9c), which is highly similar to that shown in Fig. 3. Significant anomalies of 850-hPa meridional winds and southerly
376 $\langle WVT \rangle$ prevail over the key monsoonal southerly domain, lying on the western flank of SWPCGA (Figs. 9b and c). The
377 TCC between I_{IOBM} and I_{MI} is -0.33 , significant at 0.05 on interdecadal timescales, thereby linking the significant warm
378 temperature advection anomalies indicated in Fig. 4d.

379

380 One may ask how IOBM cooling induces the above-mentioned meridional seesaw pattern. Previously, we have revealed

381 that negative SSTAs over TIO may exert remote interdecadal impacts through an atmospheric bridge, i.e., vigorous
 382 convective activities around the northeast corner of TIO (Figs. 7 and 8). In effect, there exists a low-level cyclonic
 383 anomaly in situ (Fig. 9b). Such cyclonic anomaly can be interpreted as a typical Gill–Matsuno-type response (Matsuno,
 384 1966; Gill, 1980) to the regional anti-symmetric atmospheric heating caused by IOBM cooling with the coldest center
 385 located south of the equator, which is more clear within the lower levels (Fig. 9b). As a result, consistent easterly
 386 anomalies appear from SWP to its northern flank around 15°N, denoting the active role of depressed air pressure. The
 387 consistent easterly anomalies over SWP could lead to local anticyclonic wind shear anomalies (Wang et al., 2019). In
 388 such a scenario, a quasi-barotropic SWPCGA can be induced (Fig. 9c). Further, local downward motions tied to SWPCGA
 389 could induce significant upward motions to its north via a meridional overturning circulation (J. Wang et al., 2021), thus
 390 exciting a quasi-barotropic cyclonic anomaly and an anticlockwise <WVT> gyre pattern centered over Northeast China
 391 (Figs. 9a–c). Therefore, positive summertime rainfall anomalies over EAMBZ at interdecadal timescales can be induced
 392 (Fig. 9d). Notably, circulation and precipitation anomalies during the warm phase years of the IOBM (Fig. S5) highly
 393 mirror those tied to the IOBM cooling with opposite signs.

394

395 3.4 Results from CESM1 simulations

396

397 In this subsection, we use the pacemaker experimental data based on the ensemble mean of CESM1_IOPES and
 398 CESM1_LENS to validate our proposed mechanisms regarding the modulation of IOBM cooling on the interdecadal
 399 enhancement of summer EAMBZ precipitation. Considering the predominant role of southerly anomalies over the key
 400 monsoonal southerly domain, we therefore emphasize the low-level (850 hPa) atmospheric anomalies at interdecadal
 401 timescales tied to the IOBM-like SST cooling, as depicted in Fig. 10. We can observe a clearly anomalous cyclonic
 402 circulation around the northeast corner of TIO, accompanied by local positive precipitation anomalies and easterly
 403 anomalies that stretch from SWP to its northern flank, which are generally resembled those in the observation (Fig. 9). In
 404 this circumstance, a similar “north-low–south-high” meridional seesaw pattern over the Northeast China–SWP sector can
 405 be simulated to spark and sustain the enhanced EAMBZ precipitation in boreal summer (Fig. 10). In summary, by and
 406 large, the ensemble mean composite results can well reproduce the observed anomalous circulation and precipitation
 407 driven by IOBM-related SSTAs, confirming the crucial role of IOBM cooling in driving enhanced summer precipitation
 408 over EAMBZ at interdecadal timescales.

409

410 3.5 Estimation of the interdecadal variations of summer EAMBZ precipitation

411

412 In the last three subsections, we suggest that the IOBM cooling can serve as a significant oceanic modulator for increased
 413 summer EAMBZ precipitation at interdecadal timescales based on observation evidences and pacemaker experiments,
 414 and present the corresponding physical mechanisms. To estimate their steady antiphase relationship, in the following, the
 415 negative I_{IOBM} is selected to construct a physical-based empirical model by using the simple linear regression analysis and
 416 the cross-validation method (You and Jia, 2018; Chang et al., 2021; Jeong et al., 2021), representing the impact of IOBM
 417 cooling. The physical-based model is given as follows:

418

$$419 I_{EAMBZP} = \beta_0 + \beta_1 I_{IOBM} + \varepsilon, \quad (5)$$

420

421 where β_0 and β_1 are regression coefficients, and ε denotes the residuals. The time series of I_{EAMBZP} and I_{IOBM} are detrended
 422 and 11-year low-pass filtered beforehand.

423

424 Following the method of Jeong et al. (2021), a “leaving one out” cross-validation strategy is employed to determine the
425 robustness of the hindcast estimates. The normalized time series of summer I_{EAMBZP} and associated leave-one-out cross-
426 validated hindcast estimates are shown in Fig. 11. The TCC between the physical-based predicted hindcast estimates (blue
427 line) and the observed I_{EAMBZP} (red line) for 1901–2014 can reach 0.56 ($P < 0.05$), suggesting that the physical-based
428 model can well capture the interdecadal I_{EAMBZP} variations and reflect their steady relationship.

429

430 Although our proposed physical-based empirical model could confirm the concurrently intimately interdecadal
431 relationship between IOBM and EAMBZ precipitation, we should acknowledge the shortcomings of the model.
432 First, the amplitudes of the hindcast estimates are fairly lower, which cannot well capture the extreme precipitation
433 years (e.g., years around 1960; Fig. 11). Second, the simultaneous forcing of IOBM cannot be served as a predictor
434 for summertime EAMBZ precipitation variations. As such, this model inherently lacks the ability to predict the
435 interdecadal EAMBZ precipitation anomalies in advance.

436

437 4 Conclusions and discussion

438

439 EAMBZ is a peculiar domain defined from the perspective of the interplay between climatic systems (i.e., mid-latitude
440 westerly and EASM). In this study, by analysis of the long-term observational and reanalysis datasets during 1901–2014,
441 the temporal characteristics of interdecadal variations in the summer EAMBZ precipitation and associated circulation
442 background are revealed. The potential modulation of IOBM on the variations is further discussed. As a summary of our
443 major findings, Fig. 12 schematically synthesizes how IOBM-associated SST mode remotely drives the interdecadal
444 precipitation fluctuations via a tropical route.

445

446 The summer EAMBZ precipitation exhibited a salient interdecadal fluctuations, e.g., with dry summers during the periods
447 preceding 1927, 1939–1945, 1968–1982, and 1998–2010, as well as wet summers during the periods of 1928–1938,
448 1946–1967, and 2011 onwards. It is indicated that the cold airflows brought by the mid-latitude accelerated upstream
449 westerlies over the westerly-dominated domain collide and converge with the warm and humid airflows brought by the
450 enhanced southerlies over the key EASM-controlled domain, suggesting the local extratropical–tropical interplay. Further
451 diagnostic results suggest that the monsoonal southerly anomalies could be viewed as the predominant driving factor for
452 the interdecadal enhancement of EAMBZ precipitation, whereas the upstream westerlies play a secondary dynamical
453 amplification role. Such circulation anomalies are closely linked to a “north-low–south-high” meridional seesaw pattern
454 over the Northeast China–SWP sector, which provides favorable environments for the transportation of water vapor from
455 the SWP and the convergence over EAMBZ to spark enhanced summer EAMBZ precipitation at interdecadal timescales.

456

457 We further identify that, amongst the major interdecadal oceanic forcings (e.g., Atlantic multidecadal oscillation and
458 Pacific decadal oscillation), the IOBM-related SST anomaly pattern is a salient oceanic forcing for the interdecadal
459 variations of the summer EAMBZ precipitation via the Gill–Matsuno mechanism, playing an independent and critical
460 modulation role. When the cold phase of the IOBM occurs, an anomalous cyclonic circulation is excited around the
461 northeast corner of TIO in terms of the regional anti-symmetric atmospheric heating. As a response, consistent easterly
462 anomalies appear from SWP to its northern flank, leading to local anticyclonic wind shear anomalies and thus inducing a
463 SWPCGA pattern and a resultant anticlockwise gyre pattern centered over Northeast China. On interdecadal timescales,
464 such meridional seesaw pattern tied to the IOBM cooling is responsible for enhanced summer precipitation over EAMBZ
465 through linking the predominant driving factor of strengthened monsoonal southerly anomalies west of the SWPCGA
466 pattern. As such, the water vapor transportation from the SWP and the convergence over EAMBZ can be triggered to

467 induce and sustain the enhancement local precipitation. Correspondingly, a physical-based model based the negative I_{IOBM}
468 is constructed, which can well capture the interdecadal fluctuations in the EAMBZ precipitation and reflect their steady
469 relationship. Furthermore, the results based on the large ensemble experiment and the Indian Ocean pacemaker
470 experiment also confirm the crucial physical pathway linking the SST variations over TIO with the summer precipitation
471 over EAMBZ via the influence of SST variations on the aforementioned meridional seesaw pattern at interdecadal
472 timescales.

473

474 The following two points deserve further discussion. First, although results from CESM1_LENS and CESM1_IOPES
475 can reasonably confirm our proposed physical pathway of how IOBM cooling exerts a distant modulation on the
476 interdecadal enhancement of summer precipitation over EAMBZ, we can still notice the weakness of the model
477 simulations. That is, positive precipitation anomalies around the northeast corner of TIO and the easterly anomalies
478 exhibit weaker magnitudes compared to the observations (Fig. 10 vs. 7b and 9b). Besides, systematic biases exist
479 regarding the simulated positions of the upper (lower) tropospheric divergence (convergence) and negative (positive)
480 RWS anomalies (Fig. S6), manifesting themselves in the eastward displacement tendency in contrast to those around the
481 northeast corner of the TIO (Fig. 8).

482

483 Second, this study merely identifies the physical linkage between the interdecadal summer EAMBZ precipitation
484 and the contemporaneous SST mode over the TIO basin from the tropical route. Nonetheless, the contemporaneous
485 IOBM is not a predictor. According to many previous studies (e.g., Wang et al., 2015; Li et al., 2023), the physical-
486 based empirical model based on multiple predictors may better improve the forecast skill. Thus, it is urgent to find
487 out more salient precursor forcings of the lower boundary anomalies [e.g., sea ice (Han et al., 2021)] and figure out
488 associated mechanisms for interdecadal EAMBZ precipitation changes to construct an effective prediction model.

489

490 Code and data availability. The CRU time series precipitation data version 3.26 (CRU TS3.26) from CRU at the University
491 of East Anglia are available online (<https://catalogue.ceda.ac.uk/uuid/3f8944800cc48e1cbc29a5ee12d8542d>; CRU, 2022).
492 The ERSSTv5 data from the US NOAA are available from the following website:
493 <https://www1.ncdc.noaa.gov/pub/data/cmb/ersst/v5/netcdf/> (NOAA 2020). The 20CRv2c datasets from NOAA-CIRES
494 are available from the following website: https://psl.noaa.gov/data/gridded/data.20thC_ReanV2c.html (NOAA-CIRES,
495 2022). The model simulation datasets regarding CESM1_LENS are available online
496 (<https://www.cesm.ucar.edu/community-projects/lens/data-sets>; NCAR 2023). The model simulation datasets regarding
497 CESM1_IOPES are available online (<https://www.earthsystemgrid.org/dataset/ucar.cgd.cesm4.IOD-PACEMAKER.html>;
498 NCAR 2023).

499 Codes are available from the corresponding author on reasonable request.

500

501 Author contributions. YL designed the research; JW wrote the first draft of the paper; FC and CS downloaded and
502 analyzed the data, and plotted the figures used in this study. All authors, including QL, YD, and XX, contributed to the
503 discussion of the results and reviewed the manuscript.

504

505 Competing interests. The contact author has declared that none of the authors has any competing interests.

506

507 Disclaimer. Publisher's note: Copernicus Publications remains neutral with regard to jurisdictional claims made in the
508 text, published maps, institutional affiliations, or any other geographical representation in this paper. While Copernicus
509 Publications makes every effort to include appropriate place names, the final responsibility lies with the authors.

510

511 Acknowledgements. Yanju Liu acknowledges the support by the Key Innovation Team of China Meteorological
512 Administration “Climate Change Detection and Response” (CMA2022ZD03).

513

514 Financial support. This study was supported by the Second Tibetan Plateau Scientific Expedition and Research (STEP)
515 program (2019QZKK010204-02 and 2019QZKK0102), Guangdong Major Project of Basic and Applied Basic Research
516 (2020B0301030004), and Innovation and Development Special Project of China Meteorological Administration
517 (CXFZ2022J039).

518

519 References

520

521 Chang, L., Wu, Z. and Xu, J., 2021. Contribution of Northeastern Asian stratospheric warming to subseasonal prediction
522 of the early winter haze pollution in Sichuan Basin, China. *Science of the Total Environment*, 751: 141823.

523 Chen, F.-H., Chen, J.-H., Holmes, J., Boomer, I., Austin, P., Gates, J.B., Wang, N.-L., Brooks, S.J. and Zhang, J.-W., 2010.
524 Moisture changes over the last millennium in arid central Asia: a review, synthesis and comparison with monsoon
525 region. *Quaternary Science Reviews*, 29(7): 1055-1068.

526 Chen, J., Huang, W., Feng, S., Zhang, Q., Kuang, X., Chen, J. and Chen, F., 2021. The modulation of westerlies-monsoon
527 interaction on climate over the monsoon boundary zone in East Asia. *International Journal of Climatology*,
528 41(S1): E3049-E3064.

529 Chen, J., Huang, W., Jin, L., Chen, J., Chen, S. and Chen, F., 2018. A climatological northern boundary index for the East
530 Asian summer monsoon and its interannual variability. *Science China Earth Sciences*, 61(1): 13-22.

531 Compo, G.P., Whitaker, J.S., Sardeshmukh, P.D., Matsui, N., Allan, R.J., Yin, X., Gleason, B.E., Vose, R.S., Rutledge, G.,
532 Bessemoulin, P., Brönnimann, S., Brunet, M., Crouthamel, R.I., Grant, A.N., Groisman, P.Y., Jones, P.D., Kruk,
533 M.C., Kruger, A.C., Marshall, G.J., Maugeri, M., Mok, H.Y., Nordli, Ø., Ross, T.F., Trigo, R.M., Wang, X.L.,
534 Woodruff, S.D. and Worley, S.J., 2011. The Twentieth Century Reanalysis Project. *Quarterly Journal of the Royal
535 Meteorological Society*, 137(654): 1-28.

536 CRU: CRU TS3.26, monthly, CRU [data set] <https://catalogue.ceda.ac.uk/uuid/3f8944800cc48e1cbc29a5ee12d8542d>,
537 last access: 5 July 2022.

538 Ding, Y. and Chan, J.C.L., 2005. The East Asian summer monsoon: an overview. *Meteorology and Atmospheric Physics*,
539 89(1): 117-142.

540 Dou, J. and Wu, Z., 2018. Southern Hemisphere origins for interannual variations of snow cover over the western Tibetan
541 Plateau in boreal summer. *Journal of Climate*, 31(19): 7701-7718.

542 Duchon, C.E., 1979. Lanczos filtering in one and two dimensions. *Journal of Applied Meteorology and Climatology*,
543 18(8): 1016-1022.

544 Gill, A.E., 1980. Some simple solutions for heat-induced tropical circulation. *Quarterly Journal of the Royal
545 Meteorological Society*, 106(449): 447-462.

546 Han, T., Zhang, M., Zhu, J., Zhou, B. and Li, S., 2021. Impact of early spring sea ice in Barents Sea on midsummer
547 rainfall distribution at Northeast China. *Climate Dynamics*, 57(3): 1023-1037.

548 Han, W., Vialard, J., McPhaden, M.J., Lee, T., Masumoto, Y., Feng, M. and de Ruijter, W.P.M., 2014. Indian Ocean
549 decadal variability: A review. *Bulletin of the American Meteorological Society*, 95(11): 1679-1703.

550 Harris, I., Jones, P.D., Osborn, T.J. and Lister, D.H., 2014. Updated high-resolution grids of monthly climatic
551 observations—the CRU TS3.10 Dataset. *International Journal of Climatology*, 34(3): 623-642.

552 Henley, B.J., Gergis, J., Karoly, D.J., Power, S., Kennedy, J. and Folland, C.K., 2015. A Tripole Index for the Interdecadal
553 Pacific Oscillation. *Climate Dynamics*, 45(11): 3077-3090.

554 Huang, B., Thorne, P.W., Banzon, V.F., Boyer, T., Chepurin, G., Lawrimore, J.H., Menne, M.J., Smith, T.M., Vose, R.S.
555 and Zhang, H.-M., 2017. Extended Reconstructed Sea Surface Temperature, version 5 (ERSSTv5): Upgrades,
556 validations, and intercomparisons. *Journal of Climate*, 30(20): 8179-8205.

557 Huang, J., Li, Y., Fu, C., Chen, F., Fu, Q., Dai, A., Shinoda, M., Ma, Z., Guo, W., Li, Z., Zhang, L., Liu, Y., Yu, H., He,
558 Y., Xie, Y., Guan, X., Ji, M., Lin, L., Wang, S., Yan, H. and Wang, G., 2017. Dryland climate change: Recent
559 progress and challenges. *Reviews of Geophysics*, 55(3): 719-778.

560 Huang, J., Ma, J., Guan, X., Li, Y. and He, Y., 2019. Progress in semi-arid climate change studies in China. *Advances in
561 Atmospheric Sciences*, 36(9): 922-937.

562 Huang, J., Zhang, G., Zhang, Y., Guan, X., Wei, Y. and Guo, R., 2020. Global desertification vulnerability to climate
563 change and human activities. *Land Degradation & Development*, 31(11): 1380-1391.

564 Huang, W., Chen, J., Zhang, X., Feng, S. and Chen, F., 2015. Definition of the core zone of the “westerlies-dominated
565 climatic regime”, and its controlling factors during the instrumental period. *Science China Earth Sciences*, 58(5):
566 676-684.

567 Huang, Y., Wu, B., Li, T., Zhou, T. and Liu, B., 2019. Interdecadal Indian Ocean basin mode driven by interdecadal
568 Pacific oscillation: A season-dependent growth mechanism. *Journal of Climate*, 32(7): 2057-2073.

569 Hurrell, J.W., Holland, M.M., Gent, P.R., Ghan, S., Kay, J.E., Kushner, P.J., Lamarque, J.F., Large, W.G., Lawrence, D.,
570 Lindsay, K., Lipscomb, W.H., Long, M.C., Mahowald, N., Marsh, D.R., Neale, R.B., Rasch, P., Vavrus, S.,
571 Vertenstein, M., Bader, D., Collins, W.D., Hack, J.J., Kiehl, J. and Marshall, S., 2013. The Community Earth
572 System Model: A framework for collaborative research. *Bulletin of the American Meteorological Society*, 94(9):
573 1339-1360.

574 Jeong, J.I., Park, R.J., Yeh, S.-W. and Roh, J.-W., 2021. Statistical predictability of wintertime PM_{2.5} concentrations over
575 East Asia using simple linear regression. *Science of the Total Environment*, 776: 146059.

576 Jiang, J., Zhou, T., Chen, X. and Wu, B., 2021. Central Asian precipitation shaped by the tropical Pacific decadal
577 variability and the Atlantic multidecadal variability. *Journal of Climate*, 34(18): 7541-7553.

578 Kay, J.E., Deser, C., Phillips, A., Mai, A., Hannay, C., Strand, G., Arblaster, J.M., Bates, S.C., Danabasoglu, G., Edwards,
579 J., Holland, M., Kushner, P., Lamarque, J.F., Lawrence, D., Lindsay, K., Middleton, A., Munoz, E., Neale, R.,
580 Oleson, K., Polvani, L. and Vertenstein, M., 2015. The community earth system model (CESM) large ensemble
581 project: a community resource for studying climate change in the presence of internal climate variability. *Bulletin*
582 *of the American Meteorological Society*, 96(8): 1333-1349.

583 Klein, S.A., Soden, B.J. and Lau, N.-C., 1999. Remote sea surface temperature variations during ENSO: evidence for a
584 tropical atmospheric bridge. *Journal of Climate*, 12(4): 917-932.

585 Li, J., Sun, C. and Jin, F.-F., 2013. NAO implicated as a predictor of Northern Hemisphere mean temperature multidecadal
586 variability. *Geophysical Research Letters*, 40(20): 5497-5502.

587 Li, J. and Zeng, Q., 2002. A unified monsoon index. *Geophysical Research Letters*, 29(8): 115-1-115-4.

588 Li, J., Zheng, C., Yang, Y., Lu, R. and Zhu, Z., 2023. Predictability of spatial distribution of pre-summer extreme
589 precipitation days over southern China revealed by the physical-based empirical model. *Climate Dynamics*,
590 61(5): 2299-2316.

591 Li, M. and Ma, Z., 2018. Decadal changes in summer precipitation over arid northwest China and associated atmospheric
592 circulations. *International Journal of Climatology*, 38(12): 4496-4508.

593 Lu, W. and Jia, G., 2013. Fluctuation of farming-pastoral ecotone in association with changing East Asia monsoon climate.
594 *Climatic Change*, 119(3): 747-760.

595 Mastyo, M., 2013. Bilinear interpolation theorems and applications. *Journal of Functional Analysis*, 265(2): 185-207.

596 Matsuno, T., 1966. Quasi-geostrophic motions in the equatorial area. *Journal of the Meteorological Society of Japan*,
597 44(1): 25-43.

598 Moss, R.H., Edmonds, J.A., Hibbard, K.A., Manning, M.R., Rose, S.K., van Vuuren, D.P., Carter, T.R., Emori, S.,
599 Kainuma, M., Kram, T., Meehl, G.A., Mitchell, J.F.B., Nakicenovic, N., Riahi, K., Smith, S.J., Stouffer, R.J.,
600 Thomson, A.M., Weyant, J.P. and Wilbanks, T.J., 2010. The next generation of scenarios for climate change
601 research and assessment. *Nature*, 463(7282): 747-756.

602 NCAR: CESM1_LENS, monthly, NCAR [data set] <https://www.cesm.ucar.edu/community-projects/lens/data-sets>, last
603 access: 28 April 2023.

604 NCAR: CESM1_IOPES, monthly, NCAR [data set] [https://www.earthsystemgrid.org/dataset/ucar.cgd.cesm4.IOD-](https://www.earthsystemgrid.org/dataset/ucar.cgd.cesm4.IOD-PACEMAKER.html)
605 [PACEMAKER.html](https://www.earthsystemgrid.org/dataset/ucar.cgd.cesm4.IOD-PACEMAKER.html), last access: 4 May 2023.

606 NOAA: ERSSTv5, monthly, NOAA [data set] <https://www1.ncdc.noaa.gov/pub/data/cmb/ersst/v5/netcdf/>, last access: 15
607 October 2020.

608 NOAA-CIRES: 20CRv2c, monthly, NOAA-CIRES [data set]
609 https://psl.noaa.gov/data/gridded/data.20thC_ReanV2c.html, last access: 26 June 2022.

610 North, G.R., Bell, T.L., Cahalan, R.F. and Moeng, F.J., 1982. Sampling errors in the estimation of empirical orthogonal
611 functions. *Monthly Weather Review*, 110(7): 699-706.

612 Ou, T.H. and Qian, W.H., 2006. Vegetation variations along the monsoon boundary zone in East Asia. *Chinese Journal of*
613 *Geophysics (in Chinese)*, 49(3): 698-705.

614 Piao, J., Chen, W. and Chen, S., 2021. Water vapour transport changes associated with the interdecadal decrease in the
615 summer rainfall over Northeast Asia around the late-1990s. *International Journal of Climatology*, 41(S1): E1469-
616 E1482.

617 Qian, W., Ding, T., Hu, H., Lin, X. and Qin, A., 2009. An overview of dry-wet climate variability among monsoon-
618 westerly regions and the monsoon northernmost marginal active zone in China. *Advances in Atmospheric*

619 Sciences, 26(4): 630-641.

620 Sardeshmukh, P.D. and Hoskins, B.J., 1988. The generation of global rotational flow by steady idealized tropical
621 divergence. *Journal of Atmospheric Sciences*, 45(7): 1228-1251.

622 Schiemann, R., Lüthi, D. and Schär, C., 2009. Seasonality and interannual variability of the westerly jet in the Tibetan
623 Plateau region. *Journal of Climate*, 22(11): 2940-2957.

624 Schneider, D.P. and Deser, C., 2018. Tropically driven and externally forced patterns of Antarctic sea ice change:
625 reconciling observed and modeled trends. *Climate Dynamics*, 50(11): 4599-4618.

626 Schneider, D.P., Deser, C. and Fan, T., 2015. Comparing the impacts of tropical SST variability and polar stratospheric
627 ozone loss on the southern ocean westerly winds. *Journal of Climate*, 28(23): 9350-9372.

628 Si, D. and Ding, Y., 2016. Oceanic forcings of the interdecadal variability in East Asian summer rainfall. *Journal of*
629 *Climate*, 29(21): 7633-7649.

630 Si, D., Jiang, D., Hu, A. and Lang, X., 2021. Variations in northeast Asian summer precipitation driven by the Atlantic
631 multidecadal oscillation. *International Journal of Climatology*, 41(3): 1682-1695.

632 Song, C., Wang, J., Liu, Y., Zhang, L., Ding, Y., Li, Q., Shen, X., Song, Y. and Yan, Y., 2022. Toward role of westerly-
633 monsoon interplay in linking interannual variations of late spring precipitation over the southeastern Tibetan
634 Plateau. *Atmospheric Science Letters*, 23(3): e1074.

635 Sun, B., Li, H. and Zhou, B., 2019a. Interdecadal variation of Indian Ocean basin mode and the impact on Asian summer
636 climate. *Geophysical Research Letters*, 46(21): 12388-12397.

637 Sun, B., Wang, H., Zhou, B. and Li, H., 2019b. Interdecadal variation in the synoptic features of mei-yu in the Yangtze
638 River valley region and relationship with the Pacific decadal oscillation. *Journal of Climate*, 32(19): 6251-6270.

639 Taylor, K.E., Stouffer, R.J. and Meehl, G.A., 2012. An overview of CMIP5 and the experiment design. *Bulletin of the*
640 *American Meteorological Society*, 93(4): 485-498.

641 Touma, D., Stevenson, S., Lehner, F. and Coats, S., 2021. Human-driven greenhouse gas and aerosol emissions cause
642 distinct regional impacts on extreme fire weather. *Nature Communications*, 12(1): 212.

643 Wang, B., Wu, Z., Li, J., Liu, J., Chang, C.-P., Ding, Y. and Wu, G., 2008. How to measure the strength of the East Asian
644 summer monsoon. *Journal of Climate*, 21(17): 4449-4463.

645 Wang, B., Xiang, B., Li, J., Webster, P.J., Rajeevan, M.N., Liu, J. and Ha, K.-J., 2015. Rethinking Indian monsoon rainfall
646 prediction in the context of recent global warming. *Nature Communications*, 6(1): 7154.

647 Wang, J., Zhu, Z.W., Qi, L., Zhao, Q.H., He, J.H. and Wang, J.X.L., 2019. Two pathways of how remote SST anomalies
648 drive the interannual variability of autumnal haze days in the Beijing–Tianjin–Hebei region, China. *Atmospheric*
649 *Chemistry and Physics*, 19(3): 1521-1535.

650 Wang, J., Liu, Y., Ding, Y. and Wu, Z., 2021. Towards influence of Arabian Sea SST anomalies on the withdrawal date of
651 Meiyu over the Yangtze-Huaihe River basin. *Atmospheric Research*, 249: 105340.

652 Wang, J., Liu, Y., Song, C., Ding, Y., Li, Q., Wu, P., Xu, Y. and Xu, X., 2022. Synergistic impacts of westerlies and
653 monsoon on interdecadal variations of late spring precipitation over the southeastern extension of the Tibetan
654 Plateau. *International Journal of Climatology*, 42(14): 7342-7361.

655 Wang, J., Liu, Y., Yang, Y., Wu, P., Yang, J., Liang, P., Song, C., Zhang, S. and Ding, Y., 2023. Impact of early winter
656 North Atlantic Oscillation on the dramatic alternation of seesaw haze intensity between late winter months in
657 the North China Plain. *Atmospheric Research*, 281: 106483.

658 Wang, L., Chen, W., Huang, G. and Zeng, G., 2017. Changes of the transitional climate zone in East Asia: past and future.
659 *Climate Dynamics*, 49(4): 1463-1477.

660 Wang, Q., Wang, L., Huang, G., Piao, J. and Chotamonsak, C., 2021. Temporal and spatial variation of the transitional
661 climate zone in summer during 1961–2018. *International Journal of Climatology*, 41(3): 1633-1648.

662 Wang, Q., Wang, L., Huang, G. and Wang, T., 2022. Mechanism of the summer rainfall interannual variability in
663 transitional climate zone in East Asia: roles of teleconnection patterns and associated moisture processes.
664 *Climate Dynamics*, <https://doi.org/10.1007/s00382-022-06618-1>.

665 Wang, Q., Huang, G., Wang, L., Piao, J., Ma, T., Hu, P., Chotamonsak, C. and Limsakul, A., 2023. Mechanism of the
666 summer rainfall variation in Transitional Climate Zone in East Asia from the perspective of moisture supply
667 during 1979–2010 based on the Lagrangian method. *Climate Dynamics*, 60(3): 1225-1238.

668 Wang, S., Huang, J., Huang, G., Luo, F., Ren, Y. and He, Y., 2022. Enhanced impacts of Indian Ocean sea surface
669 temperature on the dry/wet variations over Northwest China. *Journal of Geophysical Research: Atmospheres*,
670 127(11): e2022JD036533.

671 Wu, B., Zhou, T. and Li, T., 2016. Impacts of the Pacific–Japan and circumglobal teleconnection patterns on the
672 interdecadal variability of the East Asian summer monsoon. *Journal of Climate*, 29(9): 3253-3271.

673 Wu, G., Guan, Y., Liu, Y., Yan, J. and Mao, J., 2012. Air–sea interaction and formation of the Asian summer monsoon

674 onset vortex over the Bay of Bengal. *Climate Dynamics*, 38(1): 261-279.

675 Wu, P., Liu, Y., Ding, Y., Li, X. and Wang, J., 2022. Modulation of sea surface temperature over the North Atlantic and
676 Indian-Pacific warm pool on interdecadal change of summer precipitation over northwest China. *International*
677 *Journal of Climatology*, 42(16): 8526-8538.

678 Xie, S.-P., Hu, K., Hafner, J., Tokinaga, H., Du, Y., Huang, G. and Sampe, T., 2009. Indian Ocean capacitor effect on
679 Indo-western Pacific climate during the summer following El Niño. *Journal of Climate*, 22(3): 730-747.

680 Xing, W. and Wang, B., 2017. Predictability and prediction of summer rainfall in the arid and semi-arid regions of China.
681 *Climate Dynamics*, 49(1): 419-431.

682 Yang, D., Arblaster, J.M., Meehl, G.A., England, M.H., Lim, E.-P., Bates, S. and Rosenbloom, N., 2020. Role of tropical
683 variability in driving decadal shifts in the Southern Hemisphere summertime eddy-driven jet. *Journal of Climate*,
684 33(13): 5445-5463.

685 Yang, J., Liu, Q., Xie, S.-P., Liu, Z. and Wu, L., 2007. Impact of the Indian Ocean SST basin mode on the Asian summer
686 monsoon. *Geophysical Research Letters*, 34(2): L02708.

687 Yeh, T.-C., Dao, S.-Y. and Li, M.-T., 1959. The abrupt change of circulation over the Northern Hemisphere during June
688 and October. *The Atmosphere and the Sea in Motion*, the Rockefeller Institute Press and Oxford University Press,
689 249-267.

690 Ying, K., Jiang, D., Zheng, X., Frederiksen, C.S., Peng, J., Zhao, T. and Zhong, L., 2023. Seasonal predictable source of
691 the East Asian summer monsoon rainfall in addition to the ENSO-AO. *Climate Dynamics*, 60(7): 2459-2480.

692 You, Y. and Jia, X., 2018. Interannual variations and prediction of spring precipitation over China. *Journal of Climate*,
693 31(2): 655-670.

694 Zeng, J. and Zhang, Q., 2019. A humidity index for the summer monsoon transition zone in East Asia. *Climate Dynamics*,
695 53(9): 5511-5527.

696 Zhang, L., Han, W., Karlsruh, K.B., Meehl, G.A., Hu, A., Rosenbloom, N. and Shinoda, T., 2019. Indian Ocean
697 warming trend reduces Pacific warming response to anthropogenic greenhouse gases: An interbasin thermostat
698 mechanism. *Geophysical Research Letters*, 46(19): 10882-10890.

699 Zhang, Z., Sun, X. and Yang, X.-Q., 2018. Understanding the interdecadal variability of East Asian summer monsoon
700 precipitation: Joint influence of three oceanic signals. *Journal of Climate*, 31(14): 5485-5506.

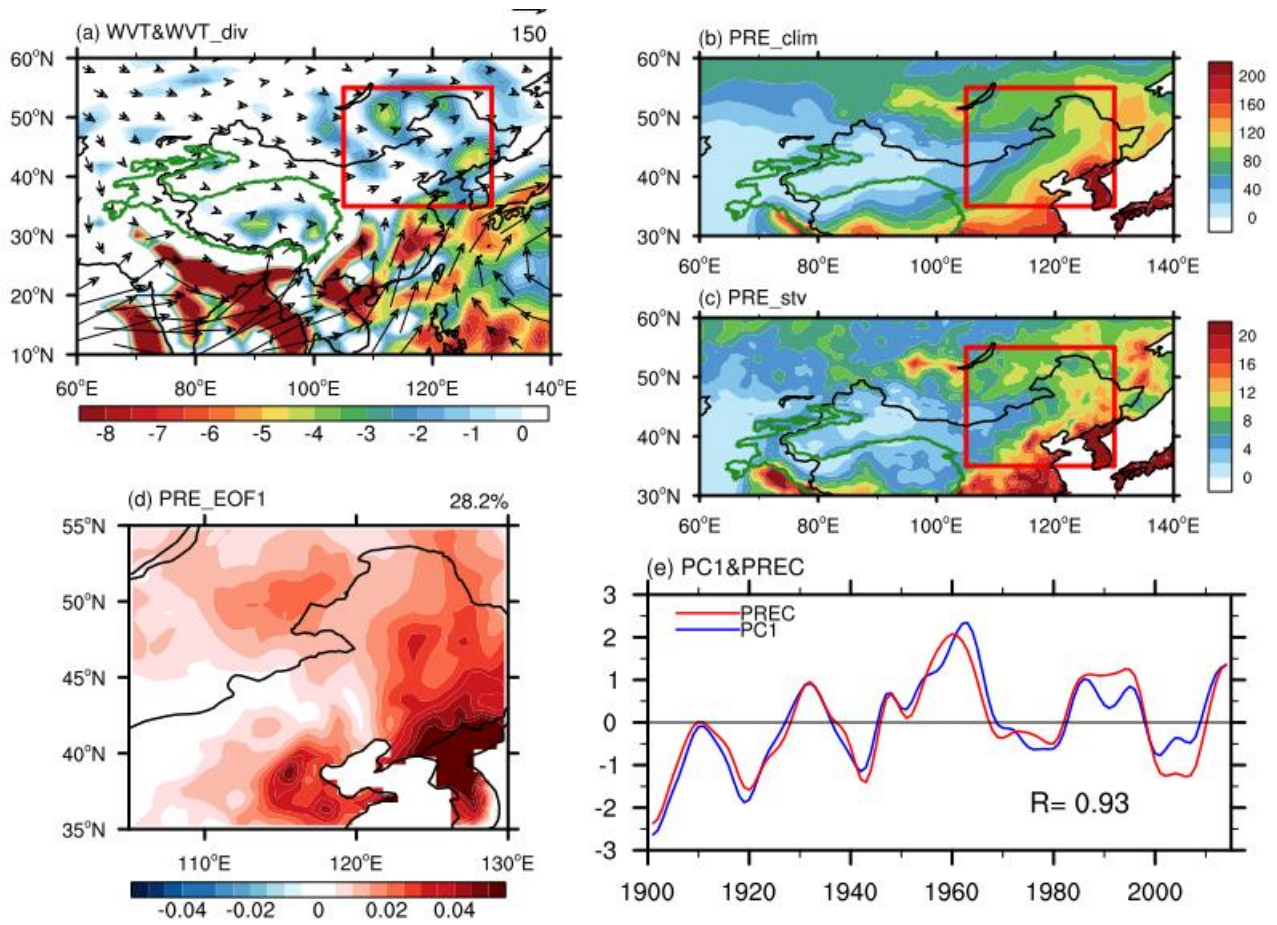
701 Zhao, W., Chen, S., Chen, W., Yao, S., Nath, D. and Yu, B., 2019a. Interannual variations of the rainy season withdrawal
702 of the monsoon transitional zone in China. *Climate Dynamics*, 53(3): 2031-2046.

703 Zhao, W., Chen, W., Chen, S., Yao, S.-L. and Nath, D., 2019b. Inter-annual variations of precipitation over the monsoon
704 transitional zone in China during August–September: Role of sea surface temperature anomalies over the
705 tropical Pacific and North Atlantic. *Atmospheric Science Letters*, 20(1): e872.

706 Zhao, W., Chen, W., Chen, S., Nath, D. and Wang, L., 2020. Interdecadal change in the impact of North Atlantic SST on
707 August rainfall over the monsoon transitional belt in China around the late 1990s. *Theoretical and Applied*
708 *Climatology*, 140(1): 503-516.

709
710
711
712
713
714
715
716
717
718
719
720
721
722
723
724

725 Figures
726



727

728 Figure 1. The climatological JJA-averaged (a) $\langle WVT \rangle$ (vectors; $\text{kg m}^{-1} \text{s}^{-1}$) and $\langle WVT_div \rangle$ (shading; $10^{-5} \text{ kg m}^{-2} \text{ s}^{-1}$), (b)
729 precipitation (mm month^{-1}), and (c) interdecadal standard deviation of precipitation (mm month^{-1}) during the period 1901–2014. The
730 red box (35° – 55° N , 105° – 130° E) outlines the research domain of EAMFBZ (the same hereinafter). (d) Spatial pattern of the first
731 empirical orthogonal function (EOF1) mode of JJA-mean EAMFBZ precipitation. (e) Normalized time series of the JJA-mean EAMFBZ
732 precipitation index ($I_{EAMFBZP}$) (red line) and associated first principal component (PC1) (blue line), with the number denoting the
733 temporal correlation coefficient (TCC) between the corresponding time series. In panels (c)–(e), variables are detrended and 11-year
734 low-pass filtered. The green outline in panels (a)–(c) represents the terrain of the Tibetan Plateau (TP) at 2000 m (the same hereinafter).
735 The precipitation is derived from the CRU TS3.26 precipitation data, while other variables are from the 20CRv2c datasets.

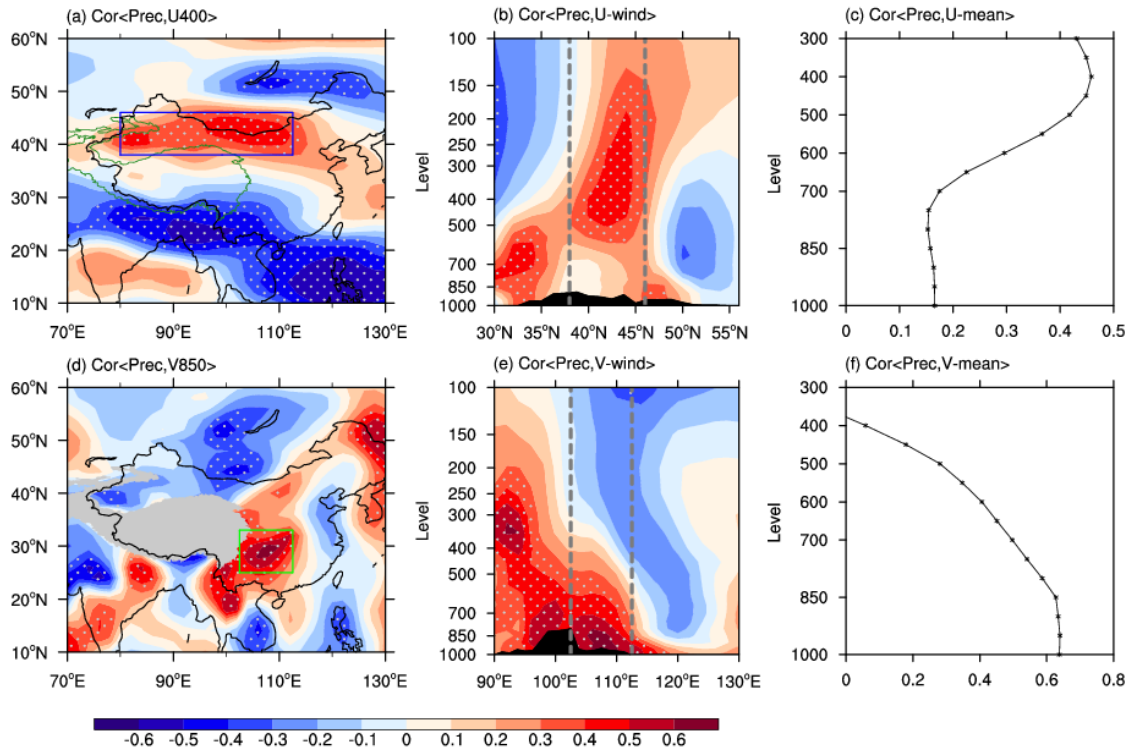
736

737

738

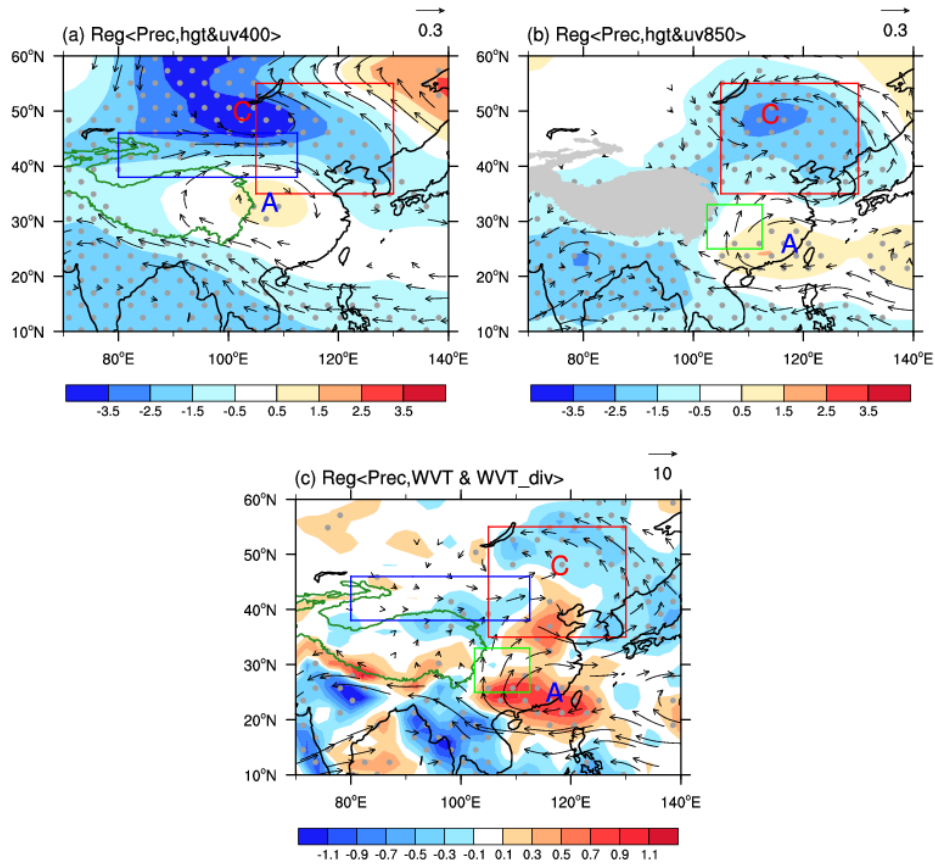
739

740



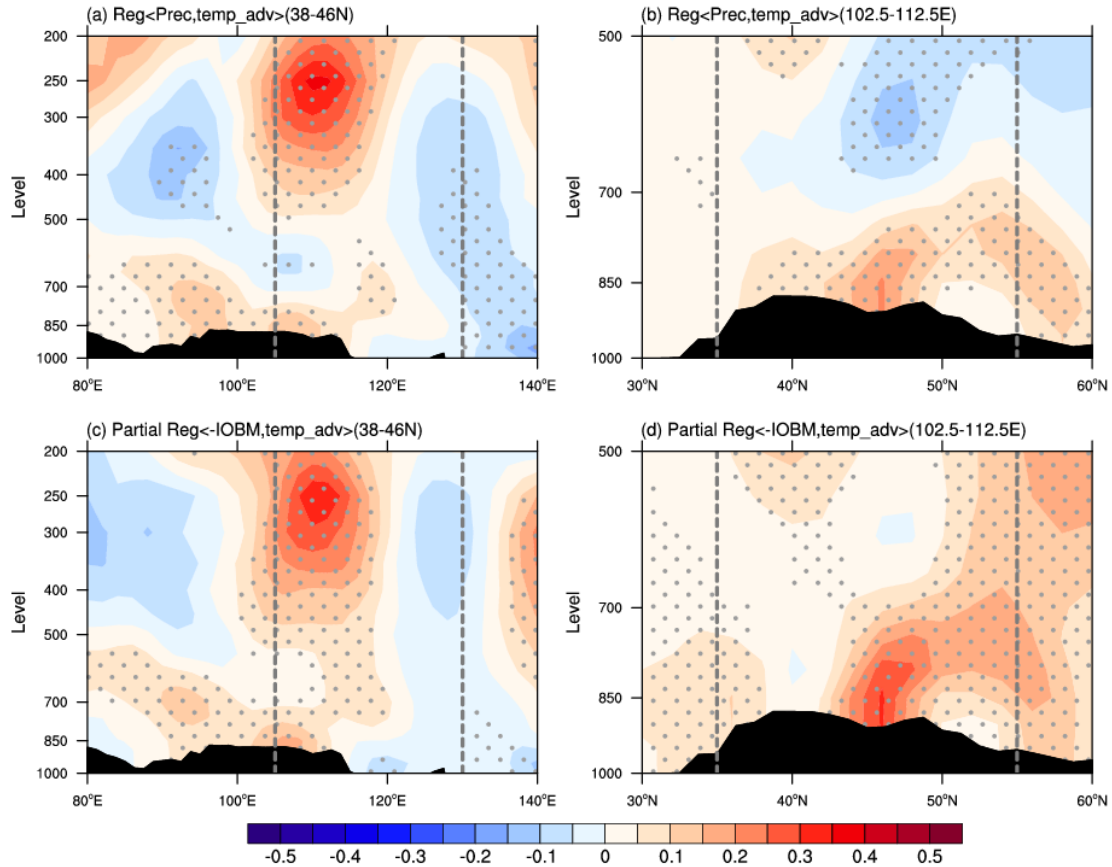
741
 742 Figure 2. Correlation maps of the JJA-averaged I_{EAMBZP} with the simultaneous (a) 400-hPa zonal wind and (d) 850-hPa meridional
 743 wind, and (b) height–latitude cross-section of zonal winds averaged over 80° – 112.5° E, and (e) height–longitude cross-section of
 744 meridional winds averaged over 25° – 33° N, during the period 1901–2014. The blue box (38° – 46° N, 80° – 112.5° E) in (a) and the green
 745 box (25° – 33° N, 102.5° – 112.5° E) in (d) represent the upstream westerly domain and the monsoonal southerly domain significantly tied
 746 to the interdecadal variations of precipitation over EAMBZ, respectively (the same hereinafter). The grey-dashed vertical lines in (b)
 747 and (e) represent the latitudinal and longitudinal range of the westerly and the monsoonal southerly domain, respectively. (c) Profile of
 748 correlation coefficients between the JJA-averaged I_{EAMBZP} and the simultaneous area-averaged zonal winds over the upstream westerly
 749 domain at multiple levels during the period 1901–2014. (f) As in (c), but for the meridional winds over the monsoonal southerly domain.
 750 All variables are detrended and 11-year low-pass filtered. Areas with significant values exceeding the 95% confidence level are stippled.
 751 The black shading indicates the topography. The grey shaded areas denote the TP areas above 2000 m (the same hereinafter). The
 752 I_{EAMBZP} is calculated based on the CRU TS3.26 precipitation data, while other variables are from the 20CRv2c datasets.

753
 754
 755
 756
 757
 758
 759
 760
 761
 762
 763



764
 765 Figure 3. Regression maps of the JJA-mean anomalies of (a) 400-hPa geopotential height (Z400; shading; m) and wind field (UV400;
 766 vectors; m s^{-1}), (b) 850-hPa geopotential height (Z850; shading; m) and wind field (UV850; vectors; m s^{-1}), and (c) $\langle \text{WVT} \rangle$ (vectors;
 767 $\text{kg m}^{-1} \text{s}^{-1}$) and $\langle \text{WVT}_{\text{div}} \rangle$ (shading; $10^{-5} \text{ kg m}^{-2} \text{s}^{-1}$) onto the concurrent I_{EAMBZP} during the period 1901–2014. All variables are
 768 detrended and 11-year low-pass filtered. Letter A (C) represents the center of anticyclonic (cyclonic) anomaly (the same hereinafter).
 769 Areas with significant values of Z400, Z850, and $\langle \text{WVT}_{\text{div}} \rangle$ that exceed the 95% confidence level are stippled, respectively. Only
 770 vectors that are significant at the 95% confidence level are shown. The I_{EAMBZP} is calculated based on the CRU TS3.26 precipitation
 771 data, while other variables are from the 20CRv2c datasets.

772
 773
 774
 775
 776
 777
 778
 779
 780
 781
 782
 783
 784



785

786

787

788

789

790

791

792

793

794

795

796

797

798

799

800

801

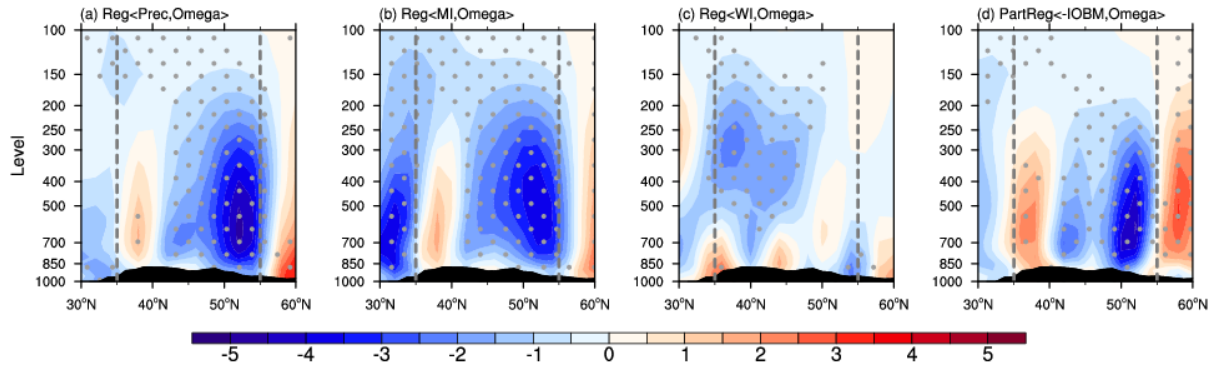
802

803

804

805

Figure 4. (a) Height–longitude cross-section (averaged over 38°–46°N) and (b) height–latitude cross-section (averaged over 102.5°–112.5°E) of the JJA-mean temperature advection anomalies (shading; 10^{-5} K s^{-1}) regressed onto the concurrent I_{EAMBZP} during the period 1901–2014. (c, d) As in (a, b), but for patterns of the partial regression coefficient between temperature advection and negative I_{IOBM} without the IPO forcing. The gray vertical lines in (a, c) and (b, d) represent the longitudinal and latitudinal range of the research domain of EAMBZ, respectively. The black shading indicates the topography. All variables are detrended and 11-year low-pass filtered. Areas with significant values exceeding the 95% confidence level are stippled. The I_{EAMBZP} and I_{IOBM}/IPO index are calculated based on the CRU TS3.26 precipitation data and the ERSSTv5 dataset, respectively; whilst other variables are from the 20CRv2c datasets.



806

807

808

809

810

811

812

813

814

815

816

817

818

819

820

821

822

823

824

825

826

827

828

829

830

831

832

833

834

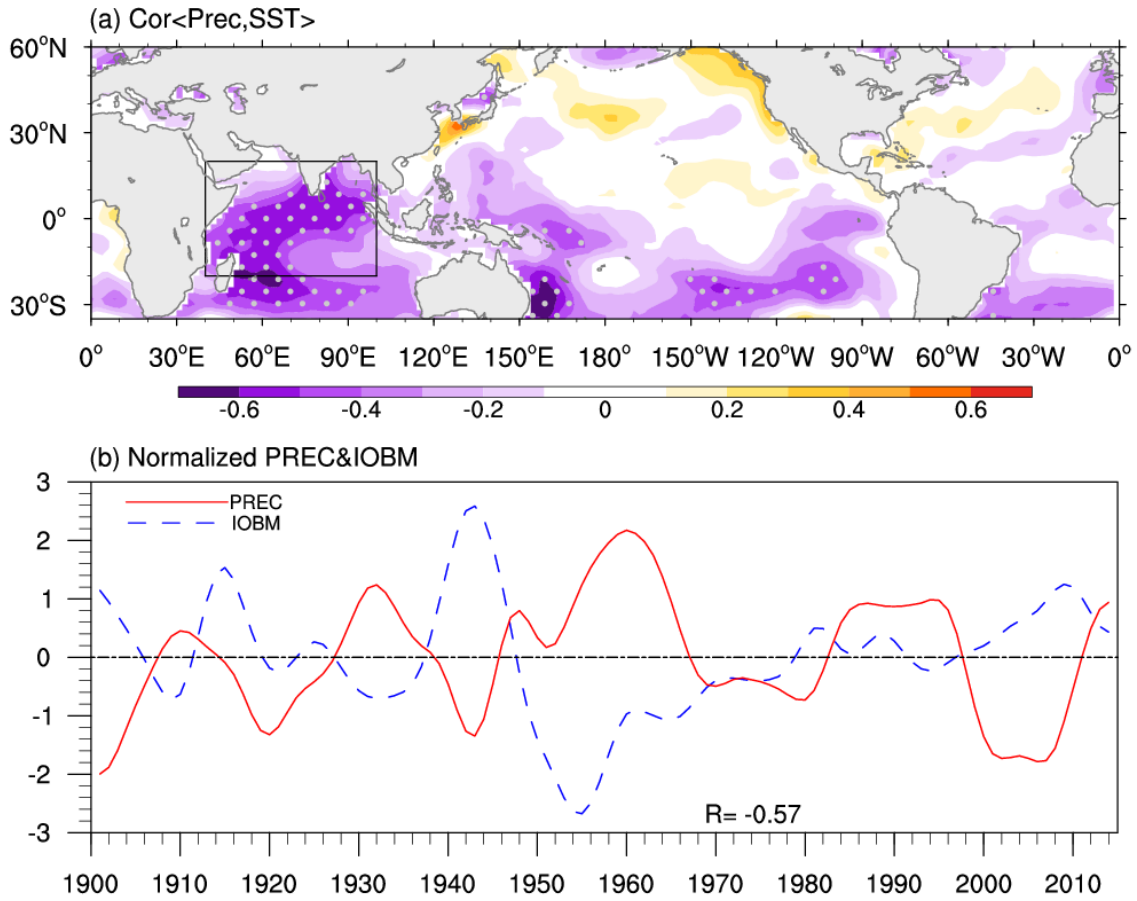
835

836

837

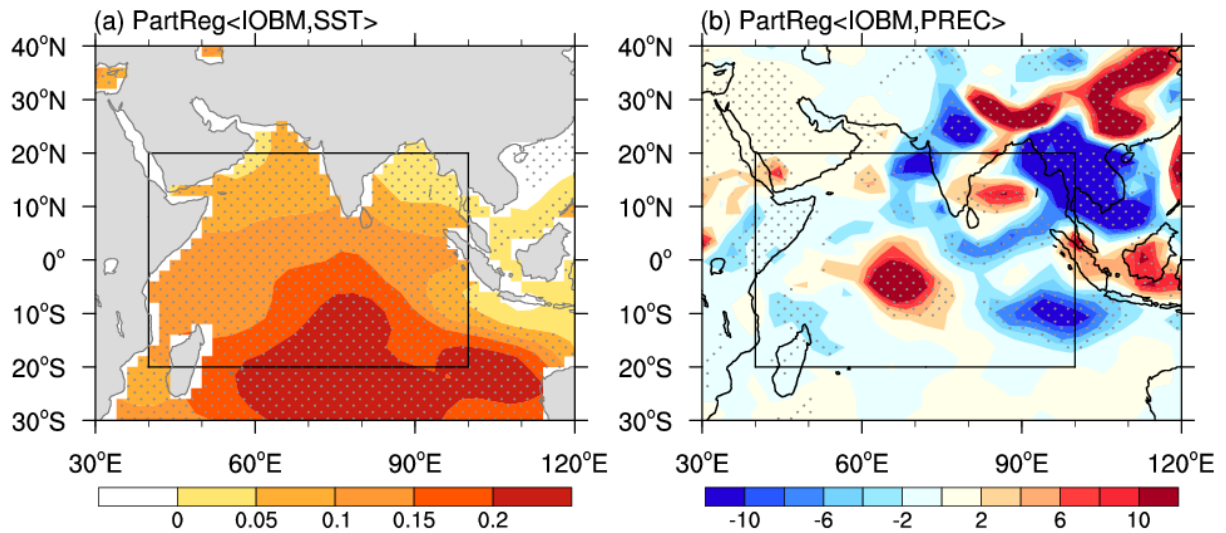
838

Figure 5. Height–latitude cross-section (averaged over 105 °–130 °E) of the JJA-mean vertical velocity anomalies ($10^{-3} \text{ Pa s}^{-1}$) regressed onto the concurrent (a) I_{EAMBZ} , (b) I_{MI} , and (c) I_{WI} during the period 1901–2014. (d) As in (a), but for the partial regressed anomalies onto the negative I_{IOBM} with the IPO forcing removed. The gray vertical lines represent the latitudinal range of EAMBZ. The black shading indicates the topography. All variables are detrended and 11-year low-pass filtered. Areas with significant values exceeding the 95% confidence level are stippled. The I_{EAMBZ} and I_{IOBM}/IPO index are calculated based on the CRU TS3.26 precipitation data and the ERSSTv5 dataset, respectively; whilst other variables are from the 20CRv2c datasets.



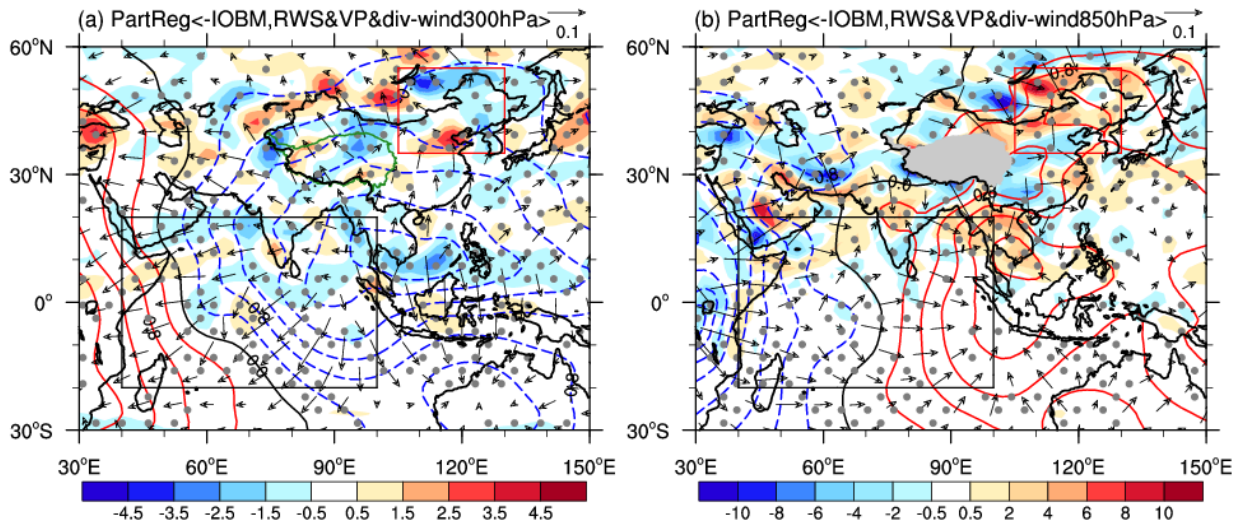
839
 840 Figure 6. (a) Correlation map of the JJA-mean I_{EAMBZP} with the concurrent near-global SST (35°S–60°N) during the period 1901–2014.
 841 The black frame (20°S–20°N, 40°E–100°E) outlines the domain for delineating the IOBM mode (the same hereinafter). Areas with
 842 significant values exceeding the 99% confidence level are stippled. (b) Normalized time series of the JJA-mean I_{EAMBZP} (red line) and
 843 I_{IOBM} (blue line) from 1901 to 2014. The numeral at the bottom represents the TCC between the corresponding time series. All variables
 844 are detrended and 11-year low-pass filtered. The SST is from the ERSSTv5 dataset. The I_{EAMBZP} and I_{IOBM} are calculated based on the
 845 CRU TS3.26 precipitation data and the ERSSTv5 datasets, respectively.

846
 847
 848
 849
 850
 851
 852
 853
 854
 855
 856
 857
 858



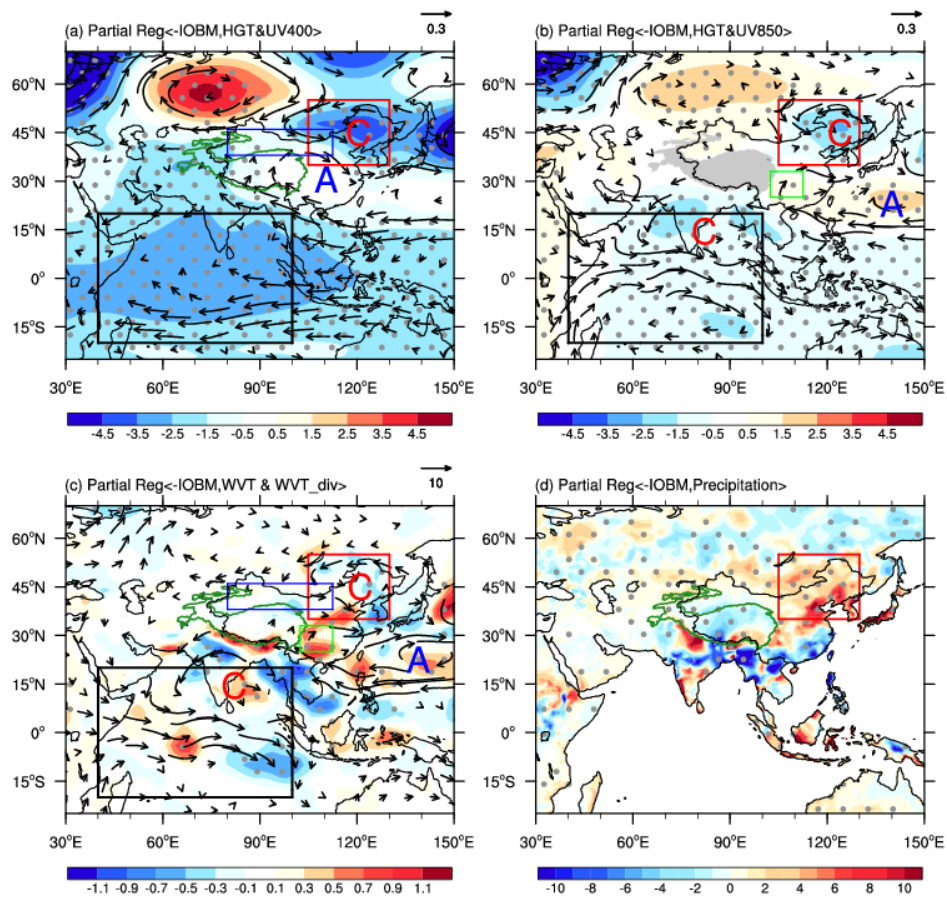
859
 860 Figure 7. Partial regression of the JJA-mean (a) SST (°C) and (b) precipitation (mm month⁻¹) anomalies over TIO and its neighboring
 861 areas onto the concurrent I_{IOBM} with the IPO forcing removed for the period 1901–2014. All variables are detrended and 11-year low-
 862 pass filtered. Areas with significant values exceeding the 95% confidence level are stippled. The I_{IOBM} /IPO index is calculated based
 863 on the ERSSTv5 dataset. The SST and the precipitation are derived from the ERSSTv5 dataset and the 20CRv2c dataset, respectively.

864
 865
 866
 867
 868
 869
 870
 871
 872
 873
 874
 875
 876
 877
 878
 879
 880



881
 882 Figure 8. Partial regression of the JJA-mean (a) 300- and (b) 850-hPa RWS (shading; 10^{-11} s^{-2}), velocity potential (contours; interval:
 883 $0.4; 10^5 \text{ m}^2 \text{ s}^{-1}$), and divergent horizontal wind (vectors; m s^{-1}) anomalies against the concurrent negative I_{IOBM} with the IPO forcing
 884 removed during the period 1901–2014. All variables are detrended and 11-year low-pass filtered. Areas with significant values of RWS
 885 exceeding the 95% confidence level are stippled. The I_{IOBM} /IPO index is calculated based on the ERSSTv5 dataset; whilst other
 886 variables are from the 20CRv2c datasets.

887
 888
 889
 890
 891
 892
 893
 894
 895
 896
 897
 898
 899
 900
 901
 902
 903
 904
 905
 906
 907
 908
 909
 910
 911
 912



913

914

915

916

917

918

919

920

921

922

923

924

925

926

927

928

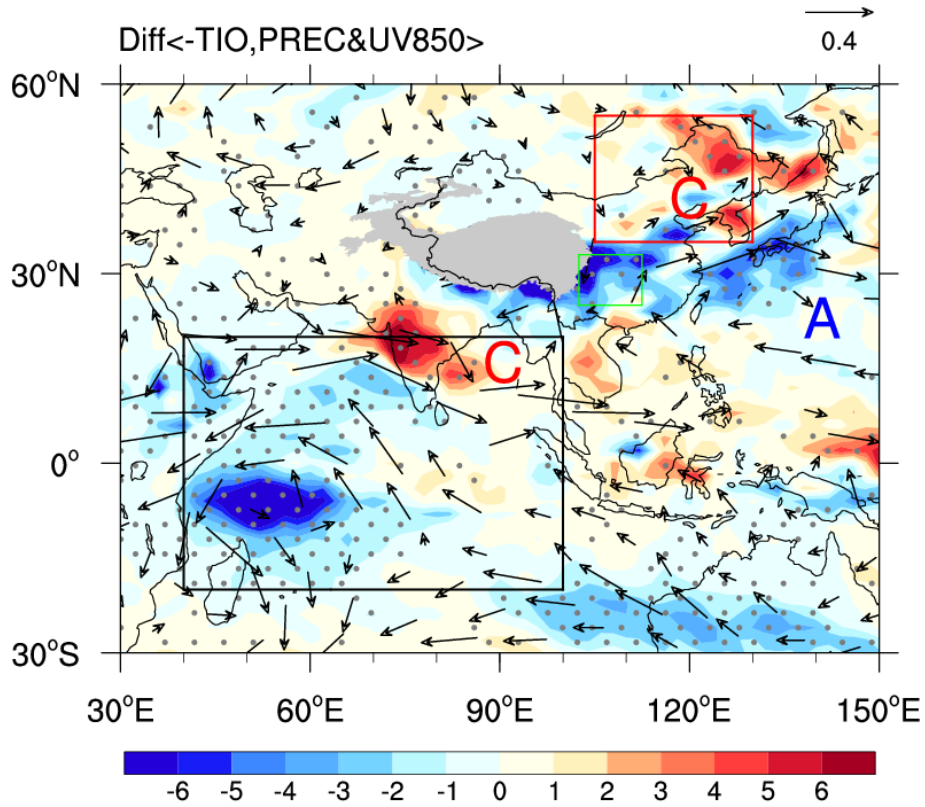
929

930

931

932

Figure 9. Partial regression of the JJA-mean (a) Z400 (shading; m) and UV400 (vectors; m s^{-1}), (b) Z850 (shading; m) and UV850 (vectors; m s^{-1}), (c) $\langle \text{WVT} \rangle$ (vectors; $\text{kg m}^{-1} \text{s}^{-1}$) and $\langle \text{WVT}_{\text{div}} \rangle$ (shading; $10^{-5} \text{ kg m}^{-2} \text{s}^{-1}$), and precipitation (mm month^{-1}) anomalies onto the concurrent negative I_{IOBM} with the IPO forcing removed during the period 1901–2014. All variables are detrended and 11-year low-pass filtered. Areas with significant values of Z400, Z850, and $\langle \text{WVT}_{\text{div}} \rangle$ that exceed the 95% confidence level are stippled, respectively. Only vectors that are significant at the 95% confidence level are shown. The I_{IOBM} /IPO index is calculated based on the ERSSTv5 dataset; the precipitation is derived from the CRU TS3.26 precipitation data; whilst other variables are from the 20CRv2c datasets.



933

934

935

936

937

938

939

940

941

942

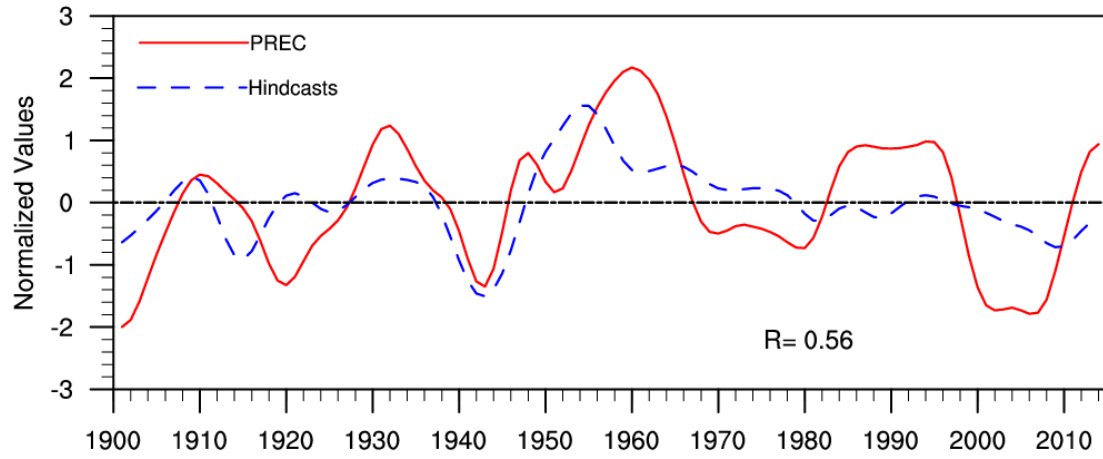
943

944

945

946

Figure 10. Simulated composite differences of JJA-mean UV850 (vectors; m s^{-1}) and precipitation (shading; mm month^{-1}) between cold and warm SST years over the broader TIO domain in CESM1_IOPES (15°S – 15°N , 40° – 174°E ; purple box in Fig. S4). The warm and cold TIO SST years are selected based on the ± 0.5 standard deviations of the simulated time-evolving SSTAs during 1920–2005, as shown in Fig. S3 (red line). All variables are detrended and 11-year low-pass filtered. Areas with significant values of precipitation that exceed the 95% confidence level are stippled. Only vectors that are significant at the 95% confidence level are shown. The simulated anomalies of UV850 and precipitation are calculated based on the difference between the CESM1_IOPES ensemble mean and the CESM1_LENS ensemble mean (former minus latter), highlighting the internally driven impacts of TIO SSTAs.



947

948

Figure 11. Normalized time series of the JJA-mean I_{EAMBZP} (red line) and associated leave-one-out cross-validated hindcast estimates (blue line) for 1901–2014, with the number denoting the TCC between the corresponding time series.

949

950

951

952

953

954

955

956

957

958

959

960

961

962

963

964

965

966

967

968

969

970

971

972

973

974

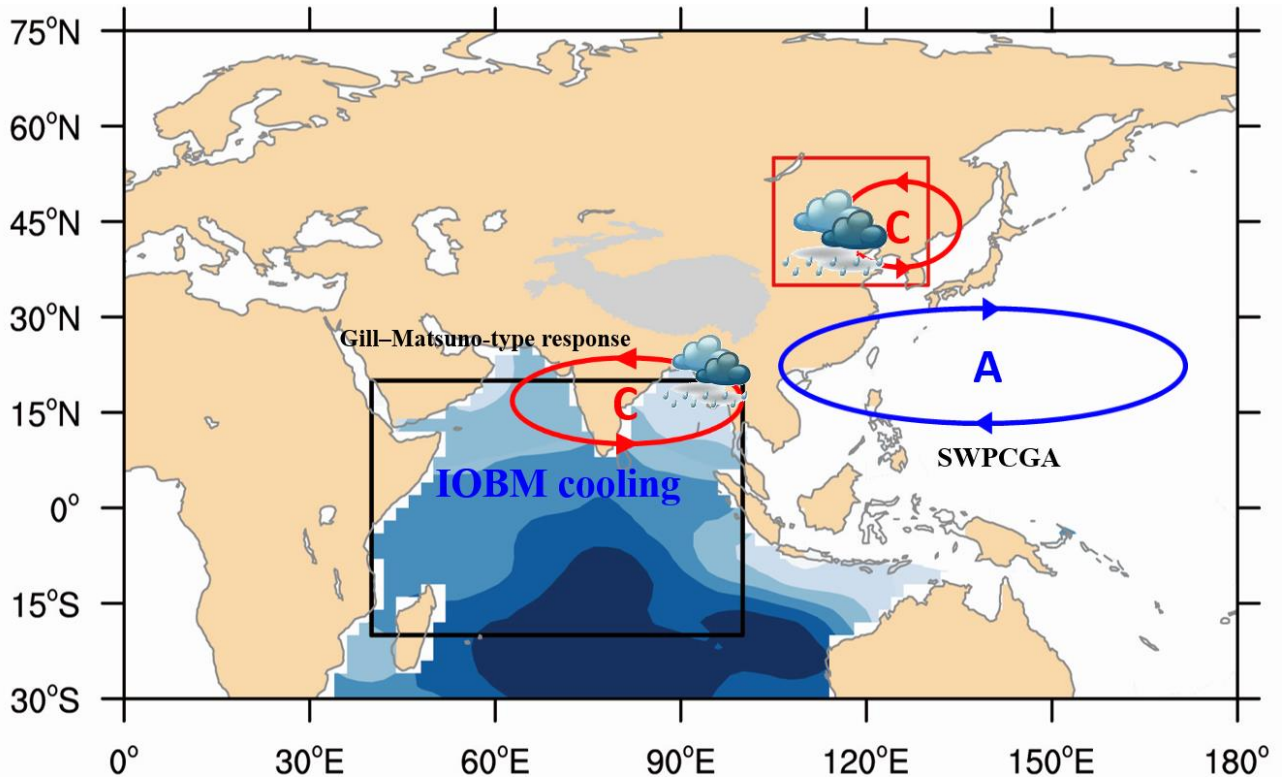
975

976

977

978

979



980

981

982

983

984

985

986

987

Figure 12. Schematic diagram showing how IOBM-related SST anomaly pattern drives the summer EAMBZ precipitation fluctuations at interdecadal timescales. Blue shading illustrates the IOBM cooling. Letter A (C) indicates the center of the anticyclonic (cyclonic) gyre anomaly.